A Simple DDES Shielding Technique to Mitigate Modeled-Stress Depletion and Promote Rapid RANS-to-LES Transition

Joshua J. Wagner*, W. Kyle Anderson†, Li Wang‡, and Veer N. Vatsa§
NASA Langley Research Center, Hampton, VA, 23681

This work presents a straightforward modification to the standard DDES shielding function that mitigates both modeled-stress depletion and delayed LES transition—two persistent challenges for hybrid RANS-LES methods. The approach centers on a new suppression function that weakens or deactivates RANS shielding when separated or detached flow is detected, based solely on the local flow orientation and the gradient of wall-normal distance. The formulation is entirely local, relying only on quantities within the solution stencil that are already available in the underlying RANS model, and it can be readily implemented into existing DDES codes. Although presented here in the context of SA-based DDES, the technique is general and amenable to alternate RANS closures. The new method is implemented in both FUN3D's finite-volume and stabilized finite-element solvers. It is first evaluated on a simple attached flow over a NACA 0012 airfoil and then on several NASA High-Lift Common Research Model (CRM-HL) configurations from the Fifth High-Lift Prediction Workshop (HLPW-5). The modification is shown to effectively mitigate modeled-stress depletion with increasing grid refinement and is compared with wall-modeled LES and wind-tunnel experiments on the CRM-HL in full landing configuration.

I. Introduction

Despite its widespread use in computational fluid dynamics (CFD) for industrial aerospace applications, traditional Reynolds-averaged Navier–Stokes (RANS) turbulence modeling remains unreliable for predicting massively separated flows, limiting its applicability across the full flight envelope [1]. Consequently, scale-resolving techniques based on large eddy simulation (LES) are needed for future CFD workflows aiming to supplant ground- and flight-testing in the design and certification of aerospace vehicles [2]. Unfortunately, resolving the energetic small-scale eddies in high-Reynolds-number turbulent boundary layers requires extremely fine grid spacing and time steps, making such simulations prohibitive even with modern computing resources. Therefore, scale-resolving simulations (SRS) at practical flight Reynolds numbers are only feasible if at least a portion of the boundary layer is modeled rather than resolved [3, 4].

Hybrid RANS/LES (HRLES) methods have emerged as a predominant strategy for alleviating the restrictive near-wall grid and time-step constraints of wall-resolved LES (WRLES) and direct numerical simulation (DNS) by modeling either the inner region or the entirety of the attached turbulent boundary layer with RANS, while selectively switching to LES to resolve the larger turbulent structures present in wakes, free shear layers, and separated flow regions. Detached-eddy simulation (DES), introduced by Spalart et al. [5], is among the most widely adopted HRLES methods, offering an effective trade-off between accuracy and computational cost and requiring only minimal modifications to existing RANS codes. DES employs a single RANS model throughout the domain that treats attached boundary layers entirely with RANS, while automatically switching its behavior to a subgrid-scale (SGS) model in separated regions. In LES mode, the turbulence model produces typical SGS dissipation by replacing the wall distance, which serves as the turbulence length scale in RANS, with a local grid length scale that characterizes the smallest resolvable eddies, resulting in an SGS formulation analogous to the Smagorinsky model [6]. The original DES method [5] was formulated with the one-equation Spalart-Allmaras (SA) turbulence model [7]; however, it has since been extended to various eddy-viscosity models, the most popular alternative being the two-equation k-ω shear-stress transport (SST) model [8–10].

Although offering significant computational savings compared to WRLES, the transition region from modeled to resolved turbulence remains a primary challenge for DES-based methods. The first problem occurs when the near-wall

---

*Research Aerospace Engineer, Computational AeroSciences Branch, AIAA Member

†Senior Research Scientist, Computational AeroSciences Branch, AIAA Associate Fellow

‡Research Aerospace Engineer, Computational AeroSciences Branch, AIAA Associate Fellow

§Distinguished Research Associate, Computational AeroSciences Branch, AIAA Associate Fellow grid spacing is fine enough to trigger LES mode inside the boundary layer but not sufficient to resolve the turbulent content needed to compensate for the reduction in modeled Reynolds stresses as the turbulence model shifts from RANS to SGS behavior. This defect, commonly known as modeled-stress depletion (MSD), produces deficient turbulent mixing, leading to an underprediction of skin friction and, ultimately, to premature separation, often termed grid-induced separation (GIS) [11]. Consequently, DES requires a narrow range of acceptable grids that are fine enough to capture key flow features and to accurately resolve the geometry but not so fine as to cause MSD. Menter and Kuntz [11] addressed the MSD issue in SST-based DES through the introduction of a shielding function that protects against spurious LES activation within attached boundary layers by leveraging the blending functions used in the SST model. Following this paradigm, Spalart et al. [12] formulated the delayed DES (DDES) method by including a shielding function applicable to the SA model, helping to delay transition to LES until outside the boundary layer. While DDES alleviates MSD and thus has essentially replaced DES in practical use, increasing compute capability now permits grids fine enough for the MSD defect to reappear despite the dedicated shielding built into DDES [13–15]. The DDES shielding function can easily be strengthened to circumvent MSD [13, 15–18]; however, if a RANS boundary layer is overprotected, the formation of instabilities in detached or separated regions will be excessively delayed [19]. This widening of the RANS-to-LES transition (RLT) region, otherwise known as the grey area, can compromise simulation accuracy in cases where the downstream unsteady dynamics are important, such as with flow reattachment [6, 14] and aeroacoustics [20–22].

Achieving enhanced DDES shielding that provides adequate RANS protection while also allowing rapid RLT remains an active area of research. Several shielding improvements have been proposed [23–31]; however, these approaches often add complexity that undermines the inherent simplicity of DDES or are less applicable to certain flow configurations, either because the underlying assumptions break down or because the computational cost becomes prohibitive. Perhaps the most prominent DDES shielding improvement to date is the universal, local formulation of Deck and Renard [32], which will be referred to herein as DDES-DR. Their approach augments the original DDES shielding function with an additional wake-layer sensor, sensitized to the negative wall-normal gradient of eddy viscosity. This added sensor provides extra RANS protection where the standard boundary-layer sensor is typically insufficient, particularly under adverse pressure gradients. A suppression (or inhibition) function, based on the wall-normal gradient of the vorticity magnitude, deactivates this additional shielding in regions with resolved vortices, preventing excessive damping of these LES structures. Together, the DDES-DR modifications allow for grid-independent shielding of attached boundary layers while maintaining rapid RLT upon separation. Renard et al. [33] later adapted the SA-based DDES-DR approach for use with the SST RANS model. Despite the success of DDES-DR, its inhibition function requires pointwise second derivatives of the velocity field, which are difficult to compute robustly on general unstructured grids because the necessary reconstructions enlarge the stencil and provide only zeroth-order accuracy [34]. Another notable approach is the local shielding function devised by Menter [26], which underlies the shielded detached eddy simulation (SDES) and stress-blended eddy simulation (SBES) methods available in the ANSYS® CFD software suite.[*] This approach appears to provide grid-independent, robust shielding and fast transition to LES; however, the formulation is proprietary and not publicly available for detailed evaluation.

This work proposes a straightforward modification to the standard DDES shielding function that addresses both the MSD and delayed RLT issues. The new method is referred to as DDES-5, representing the FUN3D development group's internal designation for the modification to the standard DDES shielding function [12], henceforth denoted as DDES-STD. As will be demonstrated, DDES-5 successfully overcomes the shortcomings of the original shielding without introducing significant additional complexity. DDES-5 employs a novel suppression function that inhibits RANS shielding in regions where the flow orientation is not aligned with the wall-parallel direction of the nearest solid surface. This suppression mechanism permits a substantial increase in shielding strength that would otherwise drastically delay the onset of LES content just downstream of separation. The DDES-5 modification requires only the local velocity vector, which is readily available, and the gradient of the wall-normal distance function, which can be easily computed from the distance function already used by the RANS model. Note that the distance function and its gradient are fixed for static grid cases and can therefore be precomputed once and stored for the duration of the simulation. DDES-5 has been incorporated into NASA Langley's FUN3D CFD software suite [35], including both its finite-volume [36] and stabilized finite-element [37] solvers. Before applying DDES-5 to several flow cases, the implications of numerical dissipation introduced by the discretization are briefly examined using the canonical inviscid Taylor-Green vortex flow. The new DDES-5 strategy is then demonstrated with a simple attached flow over a NACA 0012 airfoil, allowing for easy evaluation of the modified shielding function and its ability to protect against MSD with increasing grid refinement without widening the grey area just aft of the trailing edge. The efficacy of DDES-5 to

---

[*] Reference herein to any specific commercial product, process, or service by trade name, trademark, manufacturer, or otherwise does not necessarily constitute or imply its endorsement, recommendation, or favoring by the United States Government.

accurately simulate massively separated, strongly unsteady flow over practical aerospace configurations is then assessed for several NASA High-Lift Common Research Model (CRM-HL) cases used in the recent Fifth High-Lift Prediction Workshop (HLPW-5). DDES-5 is first shown to effectively mitigate modeled-stress depletion with increasing grid refinement on a wing-body configuration without high-lift devices (HLPW-5 Case 1), which was a defect observed in all the DDES HLPW-5 submissions for this case that did not employ either DDES-DR or DDES-SBES. The proposed method is then used for an angle-of-attack sweep on the CRM-HL full landing configuration (HLPW-5 Case 2.4) and is found to yield favorable agreement with wind-tunnel experiments and wall-modeled LES (WMLES).

II. Methodology

A. Governing Equations

The governing equations are the compressible, Reynolds-averaged Navier-Stokes equations closed with the negative SA turbulence model [38], which can be expressed in the following conservative form:

$$\frac{\partial \mathbf{Q}(\mathbf{x},t)}{\partial t} + \nabla \cdot \left(\mathbf{F}_e(\mathbf{Q}) - \mathbf{F}_v(\mathbf{Q},\nabla\mathbf{Q})\right) = \mathbf{S}(\mathbf{Q},\nabla\mathbf{Q}) \quad \text{in } \Omega\,, \tag{1}$$

where Ω is a bounded domain. The vector of conservative flow variables $\mathbf{Q}$ and the inviscid and viscous Cartesian flux vectors, $\mathbf{F}_e$ and $\mathbf{F}_v$, respectively, are defined as

$$\mathbf{Q} = \begin{bmatrix} \rho \\ \rho u \\ \rho v \\ \rho w \\ \rho E \\ \rho\tilde{\nu} \end{bmatrix}, \quad \mathbf{F}_e^x = \begin{bmatrix} \rho u \\ \rho u^2 + p \\ \rho u v \\ \rho u w \\ (\rho E + p) u \\ \rho u \tilde{\nu} \end{bmatrix}, \quad \mathbf{F}_e^y = \begin{bmatrix} \rho v \\ \rho u v \\ \rho v^2 + p \\ \rho v w \\ (\rho E + p) v \\ \rho v \tilde{\nu} \end{bmatrix}, \quad \mathbf{F}_e^z = \begin{bmatrix} \rho w \\ \rho u w \\ \rho v w \\ \rho w^2 + p \\ (\rho E + p) w \\ \rho w \tilde{\nu} \end{bmatrix}, \tag{2}$$

$$\mathbf{F}_v^x = \begin{bmatrix} 0 \\ \tau_{xx} \\ \tau_{xy} \\ \tau_{xz} \\ u\tau_{xx} + v\tau_{xy} + w\tau_{xz} + \kappa\frac{\partial T}{\partial x} \\ \frac{1}{\sigma}\rho(\nu + \tilde{\nu} f_n)\frac{\partial \tilde{\nu}}{\partial x} \end{bmatrix}, \quad \mathbf{F}_v^y = \begin{bmatrix} 0 \\ \tau_{xy} \\ \tau_{yy} \\ \tau_{yz} \\ u\tau_{xy} + v\tau_{yy} + w\tau_{yz} + \kappa\frac{\partial T}{\partial y} \\ \frac{1}{\sigma}\rho(\nu + \tilde{\nu} f_n)\frac{\partial \tilde{\nu}}{\partial y} \end{bmatrix},$$

$$\mathbf{F}_v^z = \begin{bmatrix} 0 \\ \tau_{xz} \\ \tau_{yz} \\ \tau_{zz} \\ u\tau_{xz} + v\tau_{yz} + w\tau_{zz} + \kappa\frac{\partial T}{\partial z} \\ \frac{1}{\sigma}\rho(\nu + \tilde{\nu} f_n)\frac{\partial \tilde{\nu}}{\partial z} \end{bmatrix}. \tag{3}$$

Here, ρ, p, and E denote the fluid density, pressure, and total energy per unit mass, respectively, $\mathbf{u} = (u, v, w)$ is the Cartesian velocity vector, and $\tilde{\nu}$ is the turbulence working variable in the negative SA model. The pressure p is determined by the equation of state for an ideal gas:

$$p = (\gamma - 1)\left(\rho E - \frac{1}{2}\rho\left(u^2 + v^2 + w^2\right)\right), \tag{4}$$

where γ is the ratio of specific heats, which is 1.4 for air. The viscous stress tensor τ for a Newtonian fluid is defined as

$$\tau_{ij} = (\mu + \mu_t)\left(\frac{\partial \mathbf{u}_i}{\partial \mathbf{x}_j} + \frac{\partial \mathbf{u}_j}{\partial \mathbf{x}_i} - \frac{2}{3}\frac{\partial \mathbf{u}_k}{\partial \mathbf{x}_k}\delta_{ij}\right), \tag{5}$$

where δ_{ij} is the Kronecker delta and subscripts i, j, k refer to the Cartesian coordinate components for $\mathbf{x} = (x, y, z)$. The dynamic viscosity μ is obtained via Sutherland's law [39], and the turbulent eddy viscosity μ_t is determined from the negative SA model by

$$\mu_t = \begin{cases} \rho\tilde{\nu} f_{v1} & \text{if } \ \tilde{\nu} \geq 0\,, \\ 0 & \text{if } \ \tilde{\nu} < 0\,, \end{cases} \tag{6}$$

with

$$f_{v1} = \frac{\chi^3}{\chi^3 + c_{v1}^3}\,, \quad \chi = \frac{\tilde{\nu}}{\nu}\,, \tag{7}$$

where ν is the kinematic viscosity. The thermal conductivity κ and temperature T are related to the total energy and velocity by

$$\kappa T = \gamma \left(\frac{\mu}{P_r} + \frac{\mu_t}{P_{r_t}} \right) \left(E - \frac{1}{2}\left(u^2 + v^2 + w^2\right) \right)\,, \tag{8}$$

where P_r and P_{r_t} are the meanflow and turbulent Prandtl numbers, which are set to 0.72 and 0.9, respectively. The source term in Eq. 2 is given by $\mathbf{S} = [0, 0, 0, 0, 0, S_t]^T$, where the components for the continuity, momentum and energy equations are zero. The source term corresponding to the turbulence model equation takes the following form [38]:

$$S_t = P - D + \frac{1}{\sigma} c_{b2} \rho \nabla\tilde{\nu} \cdot \nabla\tilde{\nu} - \frac{1}{\sigma}(\nu + \tilde{\nu} f_n) \nabla\rho \cdot \nabla\tilde{\nu}\,, \tag{9}$$

where the production term is given as

$$P = \begin{cases} c_{b1}\rho(1 - f_{t2})\tilde{S}\tilde{\nu} & \text{if } \ \tilde{\nu} \geq 0\,, \\ c_{b1}\rho(1 - c_{t3})S\tilde{\nu} & \text{if } \ \tilde{\nu} < 0\,, \end{cases} \tag{10}$$

and the destruction term is defined as

$$D = \begin{cases} \rho\left(c_{w1} f_w - \frac{c_{b1}}{\kappa_t^2} f_{t2}\right)\left(\frac{\tilde{\nu}}{\tilde{d}}\right)^2 & \text{if } \ \tilde{\nu} \geq 0\,, \\ -\rho c_{w_1}\left(\frac{\tilde{\nu}}{\tilde{d}}\right)^2 & \text{if } \ \tilde{\nu} < 0\,. \end{cases} \tag{11}$$

Additional definitions associated with the production and destruction terms are given as

$$\tilde{S} = \begin{cases} S + \hat{S} & \text{if } \ \hat{S} \geq -c_{v2}S\,, \\ S + \frac{S(c_{v2}^2 S + c_{v3}\hat{S})}{(c_{v3} - 2c_{v2})S - \hat{S}} & \text{if } \ \hat{S} < -c_{v2}S\,, \end{cases} \tag{12}$$

$$S = \sqrt{\boldsymbol{\omega} \cdot \boldsymbol{\omega}}\,, \quad \hat{S} = \frac{\tilde{\nu}}{\kappa_t^2 \tilde{d}^2} f_{v2}\,, \quad f_{v2} = 1 - \frac{\chi}{1 + \chi f_{v1}}\,, \quad f_{t2} = c_{t3} e^{-c_{t4}\chi^2}\,, \tag{13}$$

and

$$r = \min\left(\frac{\tilde{\nu}}{\tilde{S}\kappa_t^2 \tilde{d}^2}, r_{\text{lim}} \right), \quad g = r + c_{w2}(r^6 - r)\,, \quad f_w = g\left(\frac{1 + c_{w3}^6}{g^6 + c_{w3}^6} \right)^{1/6}\,, \tag{14}$$

where $\boldsymbol{\omega}$ is the vorticity vector and $\tilde{d}$ is the turbulent length scale. When the negative SA model operates in its typical RANS mode, $\tilde{d}$ is simply taken as the wall-normal distance function d_w. In DDES, however, $\tilde{d}$ is modified such that the RANS formulation switches to an LES-style SGS model to resolve turbulent eddies in detached flow regions, which will be discussed shortly. The negative SA model requires an additional function f_n in Eqs. 3 and 9 defined as

$$f_n = \begin{cases} 1 & \text{if } \ \tilde{\nu} \geq 0\,, \\ \frac{c_{n1} + \chi^3}{c_{n1} - \chi^3} & \text{if } \ \tilde{\nu} < 0\,. \end{cases} \tag{15}$$

The constants used above are given as $c_{b1} = 0.1355$, $\sigma = 2/3$, $c_{b2} = 0.622$, $c_{t3} = 1.2$, $c_{t4} = 0.5$, $r_{\lim} = 10$, $\kappa_t = 0.41$, $c_{w1} = c_{b1}/\kappa_t^2 + (1 + c_{b2})/\sigma$, $c_{w2} = 0.3$, $c_{w3} = 2$ $c_{v1} = 7.1$, $c_{v2} = 0.7$, $c_{v3} = 0.9$, and $c_{n1} = 16$.

Finally, some discussion of the f_{t2} parameter appearing above is warranted. The inclusion of this term was originally designed to prevent premature turbulent transition when an additional trip term, denoted as f_{t1}, was also employed [7]. In practice, the trip term is rarely included in the standard SA formulation, and its omission suggests that f_{t2} is largely unnecessary in the above equations, as noted on the NASA Turbulence Modeling Resource (TMR) website [40]. For pure RANS computations, including f_{t2} apparently has negligible effect, which likely explains why it has remained in the standard SA model despite the absence of the additional trip term. However, Vatsa et al. [41] demonstrated that in SA-based DDES for moderate Reynolds numbers and very fine grids, f_{t2} can force boundary layers to become laminar that should otherwise be fully turbulent, effectively destroying eddy viscosity and corrupting the solution in a manner similar to MSD. For this reason, all DDES cases in the current work are run fully turbulent, with the influence of the f_{t2} parameter negated by setting $c_{t3} = 0$ in both the production and destruction terms when the turbulence working variable is positive.

B. Standard Delayed Detached-Eddy Simulation (DDES-STD)

The negative SA model is converted to DDES by modification of $\tilde{d}$, which is simply equal to the wall distance d_w when the model is in standard RANS mode. In LES mode, the turbulence model functions as an SGS model by replacing $\tilde{d}$ with an approximate grid filter width. Specifically, the turbulent length scale in DDES [12] is determined by

$$\tilde{d} = d_w - f_d \max(0, d_w - C_{\text{DES}}\Delta)\,, \tag{16}$$

where f_d is the shielding function, Δ is the maximum edge length in each element, and C_{DES} is a coefficient controlling the LES filter size. Because numerical diffusion varies significantly across discretization schemes, the appropriate value of C_{DES} generally requires code-specific calibration; nevertheless, $C_{\text{DES}} = 0.65$ is a commonly used default. This topic will be discussed in further detail in Sec. III. The DDES-STD shielding function is given as

$$f_d = 1 - \tanh\left[(C_1 r_d)^{C_2}\right]. \tag{17}$$

Inspection of Eqs. (16) and (17) reveals that the shielding function preserves RANS behavior when $f_d = 0$, whereas $f_d = 1$ replaces the turbulence length scale in the negative SA model with the filter width $C_{\text{DES}}\Delta$, thereby producing LES behavior. The argument r_d is a boundary layer sensor similar to r given in Eq. 14, which is expressed as

$$r_d = \frac{\nu + \nu_t}{\sqrt{U_{i,j}U_{i,j}}\kappa_t^2 d_w^2}\,, \tag{18}$$

where $U_{i,j}$ is the velocity gradient. This value is close to unity in the logarithmic layer and vanishes outside the boundary layer.

The coefficients C_1 and C_2 in Eq. 17 control the strength of the shielding function, and their values for DDES-STD are typically set to $C_1 = 8$ and $C_2 = 3$. As mentioned in Sec. I, DDES-STD is susceptible to MSD for sufficiently fine grids. Previous studies have shown that MSD can be easily remedied by increasing C_1 to provide more robust shielding that further delays LES activation [13, 15–18]. As will be demonstrated in Sec. IV.A, indiscriminately increasing the shielding in this way will indeed protect the boundary layer, but it can also cause high levels of eddy viscosity to convect into regions of the flow that should otherwise be treated with LES. This encroachment of eddy viscosity increases the value of r_d, ultimately giving a false indication of attached boundary-layer conditions. The result is that the transition from RANS to LES is significantly delayed and the growth of otherwise resolved fluctuations in the intended LES region is suppressed.

C. Proposed Shielding Modification (DDES-5)

A simple modification to the DDES-STD shielding strategy is proposed that permits a large C_1 value for more robust protection against MSD while still allowing rapid transition to LES. The central idea of the modification is to recognize that attached boundary layers are characterized by flow approximately parallel to solid surfaces [39]. The strategy, then, is to locally weaken the shielding when the flow orientation is not well-aligned with a vector parallel to the nearest wall, suggesting the presence of detached flow. To this end, the DDES-STD shielding function is augmented with a suppression function β as follows:

$$f_d = 1 - \tanh\left[(\beta C_1 r_d)^{C_2}\right], \tag{19}$$

where $C_2 = 3$, but C_1 can now be much larger than the default value of 8. To obtain β, unit normal vectors of the local flow velocity and the wall-normal distance gradient are defined as

$$\hat{\mathbf{u}} = \frac{\mathbf{u}}{||\mathbf{u}||}, \qquad \hat{\mathbf{d}} = \frac{\nabla d_w}{||\nabla d_w||}, \tag{20}$$

respectively. Considering first a two-dimensional geometry for purposes of explanation, the unit vector perpendicular to $\hat{\mathbf{d}}$ in the plane defined by $\hat{\mathbf{d}}$ and $\hat{\mathbf{u}}$ is denoted as $\hat{\mathbf{d}}_\perp$. An illustrative example of these vectors at three different locations (A, B, and C) in a hypothetical flow is shown in Fig. 1. At location A, the flow is well-aligned with the wall-parallel direction of the closest wall boundary ($\hat{\mathbf{d}}_\perp$), in which case it is desirable to preserve strong RANS shielding and thus set the suppression function to be a value of one. The flow at location B is beginning to deviate significantly from $\hat{\mathbf{d}}_\perp$, which suggests the shielding should start to be suppressed using a value of $\beta < 1$. Finally, the flow at location C is completely separated and $\hat{\mathbf{u}}$ is strongly misaligned with $\hat{\mathbf{d}}_\perp$. For this case, the shielding should be completely suppressed with $\beta = 0$, thereby putting the model fully into LES mode. It is recognized that certain points within the detached eddies will coincidentally align with the wall; however, as will be explained shortly, the proposed shielding method avoids sporadic RANS activation at these locations, where LES is desired, by continuing to rely on the r_d sensor.

Before defining an appropriate function for β, recognize that the dot product between $\hat{\mathbf{u}}$ and $\hat{\mathbf{d}}_\perp$ yields the cosine of the angle θ between these unit vectors, which can be obtained without explicitly calculating $\hat{\mathbf{d}}_\perp$ using the following:

$$\hat{\mathbf{u}} \cdot \hat{\mathbf{d}}_\perp = \cos\theta = \sqrt{1 - \sqrt{(\hat{\mathbf{u}} \cdot \hat{\mathbf{d}})^2}}\,. \tag{21}$$

Here, the purpose of the inner square root is to effectively compute a differentiable absolute value of the dot product such that $\cos\theta \geq 0$ regardless of the direction of the flow.

Note that while the normal to the wall is well-defined in both two- and three-dimensional geometries, the direction parallel to the wall is not unique but is also never needed. As will be shown below, for purposes of computing β, any flow parallel to the wall will yield $\beta = 1$, thereby reverting the shielding to the standard DDES formulation, albeit with an increased value of C_1. In particular, $\beta = 1$ is not, by itself, sufficient in determining whether the shielding function indicates attached flow, as r_d still serves a vital role in this determination.

The suppression function is defined so that it varies smoothly from one to zero based on $\cos\theta$ using

$$\beta = 0.5(\sin\zeta + 1)\,, \tag{22}$$

where

$$\zeta = \begin{cases} \pi/2 & \text{if } \cos\theta \geq \cos\theta_{\min}\,, \\ -\pi/2 & \text{if } \cos\theta \leq \cos\theta_{\max}\,, \\ \pi\left(0.5 - \dfrac{\cos\theta - \cos\theta_{\min}}{\cos\theta_{\max} - \cos\theta_{\min}}\right) & \text{otherwise.} \end{cases} \tag{23}$$

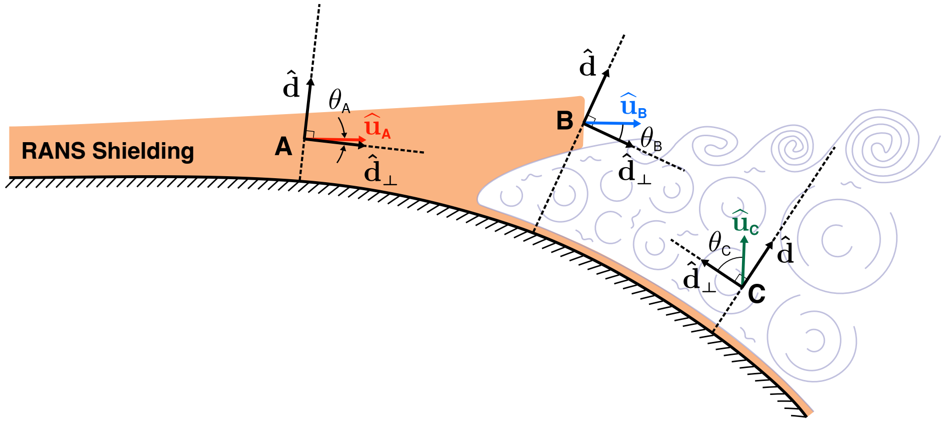

Fig. 1 Illustration demonstrating how the DDES-5 shielding-suppression function depends on the alignment of the local flow orientation with a vector perpendicular to the wall-normal distance gradient.

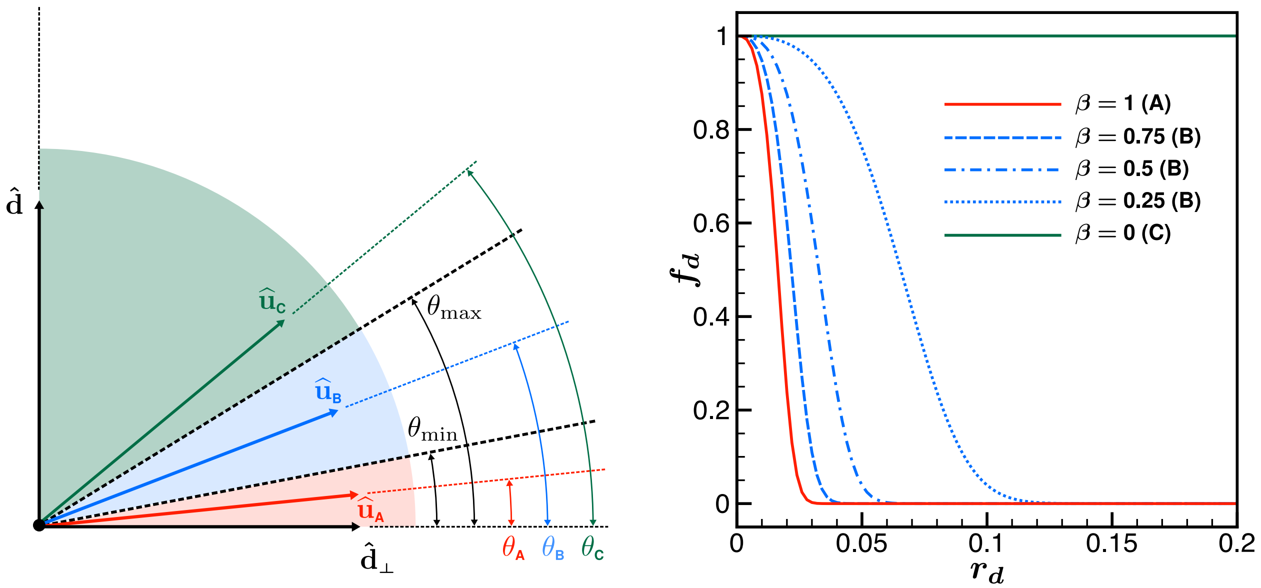

Fig. 2 Illustration demonstrating how the angle between the local flow vector and a vector perpendicular to the wall-normal distance gradient (left) modifies the shielding function with DDES-5 (right).

The parameters θ_{min} and θ_{max} are inputs that define the lower and upper limits of the range of θ where β transitions from one to zero. This concept is explained graphically in Fig. 2 for the angles depicted in Fig. 1, where the values of C_1 and C_2 are 50 and 3, respectively. The angles associated with locations A and C (θ_{A} and θ_{C}) are outside the transition wedge defined by θ_{min} and θ_{max}, and thus the suppression function yields $\beta = 1$ and $\beta = 0$, respectively. Conversely, θ_{B} is within the transition region and thus will yield a value of $0 < \beta < 1$. The effect of the suppression function on f_d at each of these locations is plotted on the right-hand side of Fig. 2. Note that for demonstration purposes, three potential scenarios at location B, all within the transition region, are illustrated in Fig. 2 (blue line types).

In Fig. 3, the suppression function is plotted with θ for various θ_{min} and θ_{max} input combinations. Notice that the plots using $\theta_{\text{min}} = 1°$ and $\theta_{\text{min}} = 5°$ are almost indistinguishable, which is the result of the argument ζ in Eq. 22 being

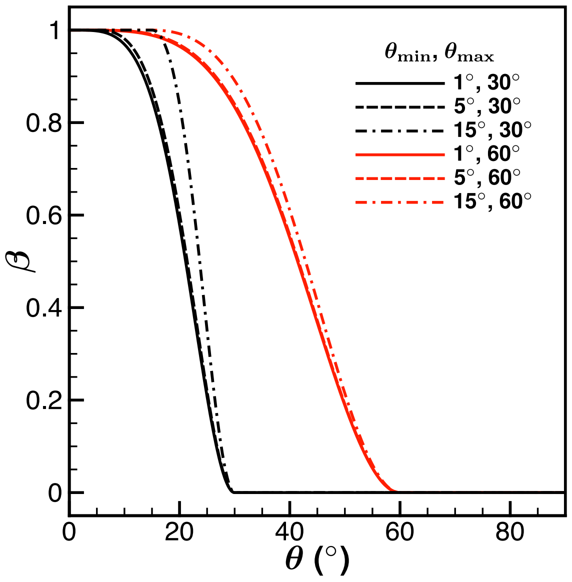

Fig. 3 Effect of the local flow angle relative to a vector perpendicular to the wall-normal distance gradient on the DDES-5 suppression function with varying θ_{min} and θ_{max} input angles.

based on the cosine of θ rather than θ itself. This choice skews the suppression function such that it decays more rapidly toward θ_{max} and is very flat near θ_{min}. Consequently, this results in a more conservative suppression function that is less sensitive to θ_{min} than it otherwise would be if the value itself were used in the formulation of ζ instead of its cosine. The default values used throughout this study are $\theta_{\text{min}} = 5^\circ$ and $\theta_{\text{max}} = 30^\circ$; however, the effect of choosing different values of θ_{max} will be examined on an actual flow case in Sec. IV.A.

The suppression function permits the use of a substantially increased C_1 value over the DDES-STD default of 8. When the flow is well-aligned with the wall direction, a defining feature of an attached boundary layer, the large C_1 value ensures uncorrupted RANS coverage over the entire boundary layer. However, it is important to reiterate that the model may still refuse RANS mode at a location where the flow is parallel to the wall ($\beta = 1$) if the r_d function is small, which might be the case for local spanwise flow or regions of detached eddies that align with a wall-parallel vector. Conversely, when the local mean flow orientation forms a large angle with the wall-parallel direction of the nearest surface, detached flow can be confidently assumed regardless of r_d. In this limit, β becomes small, suppressing C_1 and enabling LES treatment at that location. For reasons discussed in Sec. IV.A, a default value of $C_1 = 50$ is chosen for DDES-5.

D. Flow Solver

The DDES-5 modification is implemented in both the finite-volume and stabilized finite-element flow solvers in NASA Langley's FUN3D CFD software suite, herein denoted as FUN3D-FV and FUN3D-FE, respectively. Both solvers discretize the governing equations on unstructured, mixed-element grids and employ a second-order accurate backward-difference time-stepping scheme. FUN3D-FV [36] uses a node-centered spatial discretization in which the median-dual control volumes are centered on grid vertices. An approximate Riemann solver is used for the inviscid fluxes; specifically, Roe's flux-difference splitting for this work [42]. Viscous fluxes are discretized using Green–Gauss cell-based gradients. On tetrahedral grids, this is equivalent to a Galerkin approximation, while on other grid types, the cell-based gradients are blended with edge-based gradients to improve stability and prevent odd–even decoupling. These inviscid- and viscous-flux discretizations provide second-order spatial accuracy on general mixed-element unstructured grids. The FUN3D-FE solver [37] uses a streamlined upwind Petrov-Galerkin (SUPG) discretization [43] with linear (P1) elements, which is spatially second-order accurate. The solution is obtained at each time step using a subiterative procedure, where the time-dependent residual is fully linearized, and a CFL controller is used to achieve global convergence. The resulting linear system is solved with a preconditioned generalized minimal residual (GMRES) method at each subiteration [44].

III. Evaluating C_{DES} with the Inviscid Taylor-Green Vortex

LES resolves the large, energy-containing turbulent structures directly, while modeling the effects of the smaller-scale eddies that cannot be resolved by the computational grid. In LES, there are three mechanisms for damping unresolved subgrid vortices, which would otherwise lead to nonphysical accumulation of turbulent kinetic energy at high wave numbers. These mechanisms include physical molecular viscosity, numerical dissipation introduced by the discretization, and explicit dissipation provided by the SGS model. As mentioned in Sec. II.B, the C_{DES} parameter controls the size of the characteristic grid scale, which ultimately determines how much SGS dissipation the SA model should provide when operating in the LES branch of DDES. Calibration of this value is generally required for individual codes because numerical dissipation varies greatly between schemes. Therefore, C_{DES} should be chosen so that the SGS model supplies only enough additional dissipation beyond the physical and numerical damping to represent the unresolved vortices and prevent energy accumulation and spurious oscillations. The calibration is usually performed by simulating decaying isotropic turbulence (DIT) with various C_{DES} values and determining the one that best predicts the turbulent energy cascade when compared to DNS [6]. However, there are several shortcomings to this approach. First, the optimal C_{DES} value is grid-dependent, varying with both the grid resolution and element type. The DIT calibration is typically performed on grids with structured cubic cells; however, practical flow cases generally rely on irregular unstructured grids that are inherently more dissipative, especially when comprised of tetrahedral elements. Additionally, many researchers follow the hybrid upwind–central scheme of Travin et al. [9], which switches to a non-dissipative central discretization in the intended LES regions; accordingly, the calibration is usually conducted without any upwind-based dissipation. However, this hybrid approach is often not robust for complex geometries and their associated meshes. As a result, practical simulations tend to include more inherent numerical dissipation than is present during calibration. Combined with the general difficulty of setting up the DIT case, many researchers forgo calibration entirely and adopt the default value $C_{\text{DES}} = 0.65$ [45].

In the present work, the effect of numerical diffusion is isolated using an inviscid Taylor-Green vortex (TGV). For

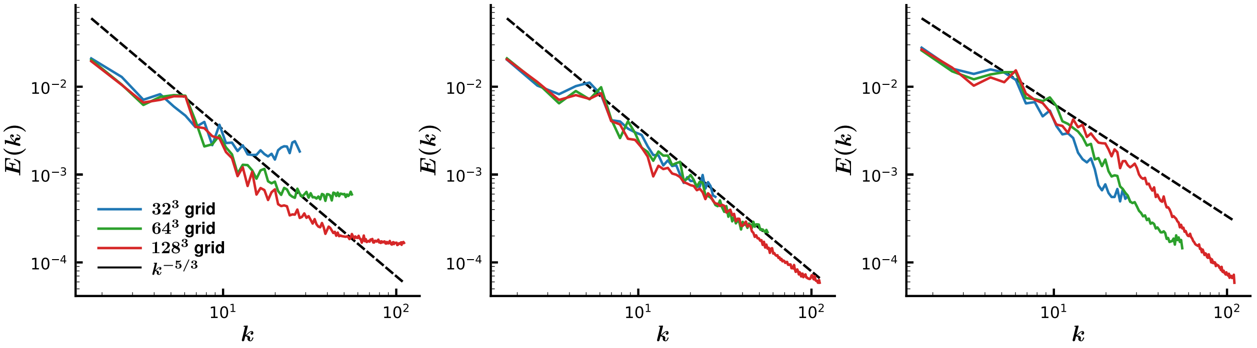

(a) $\alpha_{\mathrm{pg}} = 0.05$ (b) $\alpha_{\mathrm{pg}} = 0.2$ (c) $\alpha_{\mathrm{pg}} = 1.0$

Fig. 4 Energy spectra of the inviscid Taylor-Green vortex at t = 9 with varying grid resolution and numerical diffusion, computed with FUN3D-FE.

this case, the energy spectrum $E(k)$ obtained from the inviscid TGV flow (taken at a time when the dissipation rate is a maximum so that vortex stretching and breakdown are present) should produce a linear inertial range down to the cutoff frequency, following a $k^{-5/3}$ slope.

The initial conditions and domain for the simulations are given by Atkins [46]. The inherent symmetry of the flow is exploited, allowing for only 1/8th of the full flow field to be simulated, with symmetry conditions enforced at all boundaries. Three regular hexahedral grids with 32^3, 64^3, and 128^3 nodes are used, and the simulations are performed with FUN3D-FE. In this solver, the added SUPG dissipation is controlled by a coefficient α_{pg}, which is equal to one when the full magnitude of the stabilization term is used, zero when no numerical dissipation is added, and between zero and one for a blend of SUPG and the non-dissipative Galerkin scheme. Note that the FUN3D-FV solver has an analogous parameter κ_u to also control its numerical dissipation. The TGV simulations are run on all grids for three numerical dissipation levels $\alpha_{\mathrm{pg}} = 0.05$, 0.2, and 1.0. The resulting energy spectra sampled at a nondimensional time $t = 9$ are given in Fig. 4. In the case with minimal numerical dissipation (Fig. 4(a)), the energy "piles up" at the high wavenumbers, indicating unresolved features with insufficient dissipation. In Fig. 4(b), where $\alpha_{\mathrm{pg}} = 0.2$, the energy spectra for all grids approximately follows a $k^{-5/3}$ slope, therefore suggesting that the numerical dissipation alone is capable of damping the fine-scale vortices for this case. Finally, for $\alpha_{\mathrm{pg}} = 1.0$, shown in Fig. 4(c), the numerical dissipation is found to be excessive given that the energy spectra are over-damped in the high wavenumber range.

The takeaway from this study is that the second-order spatial discretization currently used in FUN3D-FE, as described in Sec.II.D, provides sufficient levels of dissipation to prevent energy accumulation near the cutoff wavenumber when $\alpha_{\mathrm{pg}} \geq 0.2$, thus not requiring explicit SGS dissipation. Consequently, for $\alpha_{\mathrm{pg}} \geq 0.2$, the default value of $C_{\mathrm{DES}} = 0.65$ is excessive, thus a smaller C_{DES} coefficient is usually employed that will minimize extra dissipation but still maintains general solver robustness. Based on extensive testing across a wide range of problems and mesh configurations, the authors have found that a value between $C_{\mathrm{DES}} = 0.2$ to 0.3 typically achieves this balance. Although not shown here, similar findings were obtained for the FUN3D-FV discretization used in this work when varying κ_u. Note that in both FUN3D-FE and FUN3D-FV, the strategy is to run complex flow simulations with full dissipation to get through initial transients, before reducing the dissipation for subsequent time steps. However, such an approach is obviously not relevant here given the breakdown of a TGV is entirely transient; therefore, the same dissipation parameter is used throughout each simulation.

Another important effect of lowering C_{DES} is that it accelerates the RLT by sharply reducing the eddy viscosity just after detachment [47]; however, this increases the strength of the destruction term in the SA model, which can make the solution more susceptible to MSD. Therefore, robust RANS shielding is even more critical when C_{DES} is reduced below the default value. Examples of this scenario will be given in Sec. IV.A.

IV. Results

In this section, the DDES-5 shielding modification is assessed for both simple and complex flow cases, beginning with attached flow over a NACA 0012 airfoil, followed by more practical HLPW-5 cases on the NASA CRM-HL model. The results for the first case are computed entirely with FUN3D-FV and are used to demonstrate the basic operation of DDES-5 and the effects of parameter variations. The HLPW-5 cases are run using both FUN3D-FV and

FUN3D-FE solvers and are intended to assess the method's ability to predict complex flow over practical aerodynamic configurations.

A. NACA 0012 Airfoil

In the first test case, RANS, DDES-STD, and DDES-5 are used to compute the flow over the symmetric NACA 0012 airfoil under conditions that maintain an attached boundary layer along the entire chord. Because the natural operation of DDES aims to treat the entire attached boundary layer with RANS [12], an adequately shielded DDES solution should essentially match RANS up to the trailing edge, followed by a rapid decay of eddy viscosity to LES levels in the wake. Note that while these computations could be conducted in three dimensions with periodic boundary conditions, the results would be nearly identical to their two-dimensional counterparts up to the trailing edge, as confirmed by the authors through comparison with a three-dimensional simulation (not shown here for brevity). Because the intent of this case is solely to evaluate RANS shielding for fully-attached flow, rather than to resolve turbulent dynamics, the simulations in this section are performed in two dimensions to reduce the unnecessary computational burden. Practical 3D turbulence-resolving behavior is considered in the subsequent test cases. Therefore, this simple test case serves as a convenient and inexpensive baseline problem to assess the performance of new DDES shielding methods.

The flow conditions correspond to a freestream Mach number of 0.2, chord-based Reynolds number of 5.0×10^6, and angle of attack of 3°. The blunt trailing-edge NACA 0012 geometry described on the NASA TMR website [40] is used here. The time-step size is chosen so that 1000 steps represent a single convective time unit (CTU), which is defined as the time the flow takes to travel the characteristic length c (the airfoil chord) based on the freestream velocity U_∞. The simulations are carried out on three grids with 34.1 thousand points (coarse), 75.9 thousand points (medium), and 196.7 thousand points (fine) on a single 2D plane, which are shown in Figs. 5(a), 5(b), and 5(c), respectively. Note that FUN3D only supports quasi-2D simulations requiring two y-planes; therefore, the grids are extruded in the spanwise direction to be one element thick, resulting in a mix of prismatic and hexahedral elements. The first point off the wall for each grid is placed at $\Delta y_w^+ = 1$ based on a flat-plate approximation with U_∞ and c. Subsequent spacing then grows with a rate of 1.2 until isotropic grid cells are reached. RANS solutions are obtained when the mean flow and turbulence-model residuals are reduced to machine precision. DDES simulations are advanced for 40 CTUs from freestream initial conditions, with unsteady residuals reduced by approximately five orders of magnitude by the end of

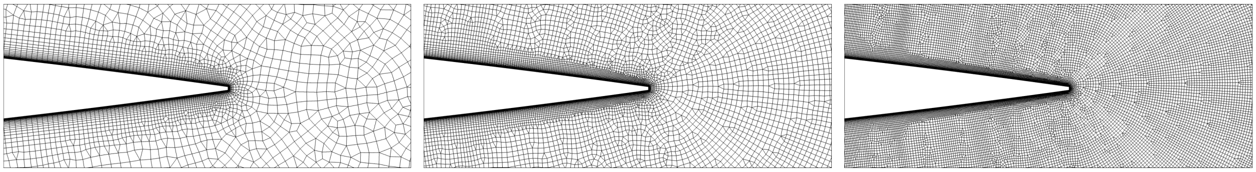

(a) Coarse grid (34.1K) (b) Medium grid (75.9K) (c) Fine grid (196.7K)

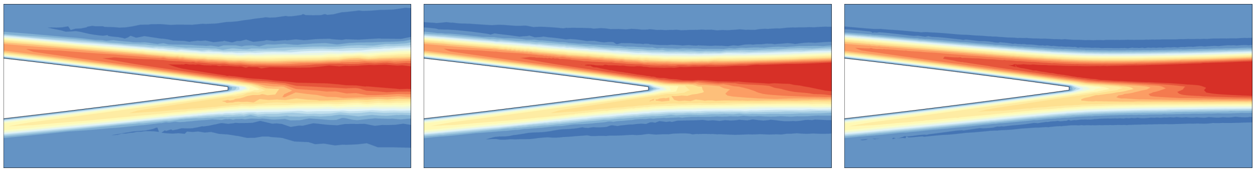

(d) RANS (34.1K) (e) RANS (75.9K) (f) RANS (196.7K)

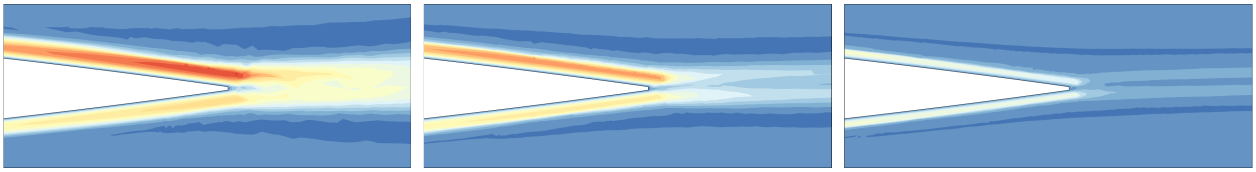

(g) DDES-STD (34.1K) (h) DDES-STD (75.9K) (i) DDES-STD (196.7K)

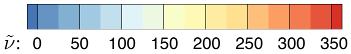

Fig. 5 Computational grids near the tailing edge of the NACA 0012 airfoil and contours of the turbulence working variable obtained with RANS and DDES-STD on each grid. Numbers in parentheses are mesh node counts in thousands.

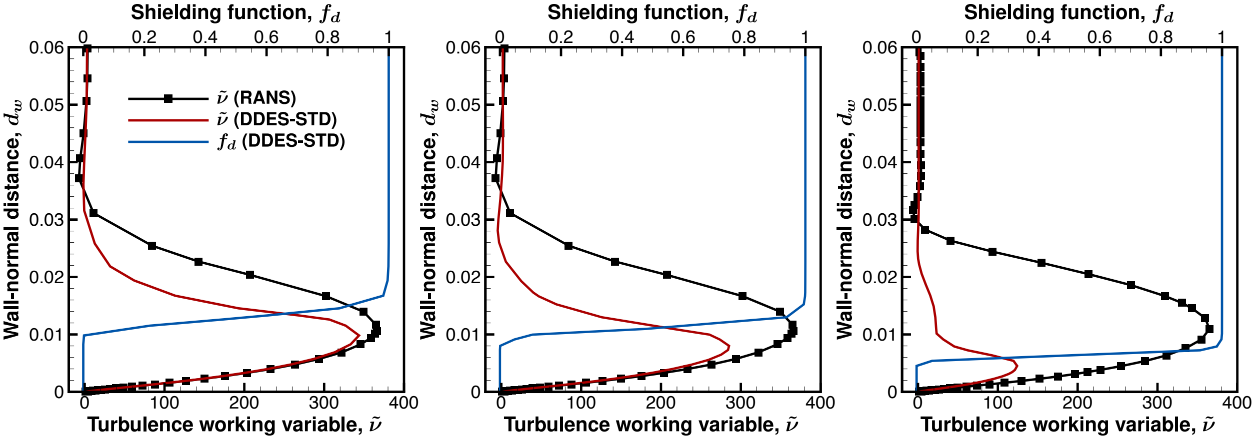

(a) Coarse grid (b) Medium grid (c) Fine grid

Fig. 6 Wall-normal profiles of the turbulence working variable and shielding function above the airfoil at $x = 0.98c$ computed with RANS and DDES-STD.

the subiterative process for each time step.

Some studies suggest that DDES simulations should be initialized from a RANS solution to ensure a valid shielding field arises, since f_d depends on the eddy viscosity [32]. However, in tests not shown here for brevity, the differences between solutions initialized from freestream conditions and those from a converged RANS solution were found to be negligible, indicating that the shielding and eddy viscosity fields can sufficiently develop even if initially lacking. Additionally, DDES-5 cases initialized from a depleted DDES-STD solution produced results that were nearly indistinguishable from both freestream- and RANS-initialized cases.

Contours of $\tilde{\nu}$ for the baseline RANS solutions on each grid are shown in Figs. 5(d)-(f), and the corresponding DDES-STD solutions computed with $C_{\mathrm{DES}} = 0.65$ are shown in Figs. 5(g)-(i). In the RANS solutions, large values of the turbulence working variable cover the boundary layer and are advected downstream into the wake. For the DDES-STD solutions, a significant reduction in $\tilde{\nu}$ is clearly visible with increasing grid resolution, highlighting the insufficient RANS protection of the standard DDES shielding function on fine grids and the resulting severe MSD. The DDES-STD results exhibit a further decay in $\tilde{\nu}$ beyond the trailing edge, confirming the model has transitioned from RANS to LES in the wake as expected. Figure 6 compares the profiles of $\tilde{\nu}$ obtained with RANS and DDES-STD along a line normal to the upper airfoil surface at $x = 0.98c$. The DDES-STD $\tilde{\nu}$ profiles deviate further from RANS as the grid becomes finer, with the maximum value significantly decreasing as the mesh is refined. Also shown in the figure is the DDES-STD shielding function f_d, which goes to one closer to the wall on the finer grids, exposing more of the boundary layer to LES activation. This breakdown in shielding arises from a destructive feedback loop stemming from the fact that the shielding depends on the eddy viscosity through the r_d parameter given in Eq. 18. Therefore, any reduction in ν_t due to insufficient RANS protection is fed back into the shielding function, driving f_d toward one deeper into the boundary layer, i.e., weakening the shielding. The cycle continues destroying the RANS coverage of the attached boundary layer until an equilibrium is reached. The effect is more pronounced on finer grids due to the enhanced turbulence destruction caused by the smaller filter width.

As mentioned previously, MSD can be avoided by simply increasing C_1 in Eq. 17. This is demonstrated in Fig. 7 where the resulting f_d and $\tilde{\nu}$ contours are shown for $C_1 = 8$, 16, and 32 on the finest grid when using $C_{\mathrm{DES}} = 0.65$. The larger coefficients provide adequate boundary-layer protection, and the $\tilde{\nu}$ contours in Figs. 7(b) and 7(c) look similar to the corresponding RANS results in Figs. 5(e)and 5(f) up to the trailing edge of the airfoil. Notice, however, that increasing C_1 extends the shielding significantly beyond the trailing edge, allowing large $\tilde{\nu}$ to be convected deeper into the wake region before it is destroyed by the DDES limiter. Therefore, indiscriminately increasing C_1 has the undesirable effect of smearing the grey area and delaying the formation of LES content in the detached region.

Recall from Sec.III, motivation was given for using a reduced C_{DES} coefficient, which was also supported by Simon et al. [47]. However, it was stressed that lowering this coefficient can exacerbate the MSD issue. To demonstrate this, the simulations shown in Fig. 7 using $C_{\mathrm{DES}} = 0.65$ are repeated with $C_{\mathrm{DES}} = 0.2$. The resulting f_d and $\tilde{\nu}$ contours on the finest grid are given in Fig. 8. As shown in Fig. 8(b), the increased coefficient $C_1 = 16$ no longer adequately shields the boundary layer when C_{DES} is lowered to 0.2; however, Fig. 8(c) confirms $C_1 = 32$ still provides sufficient RANS

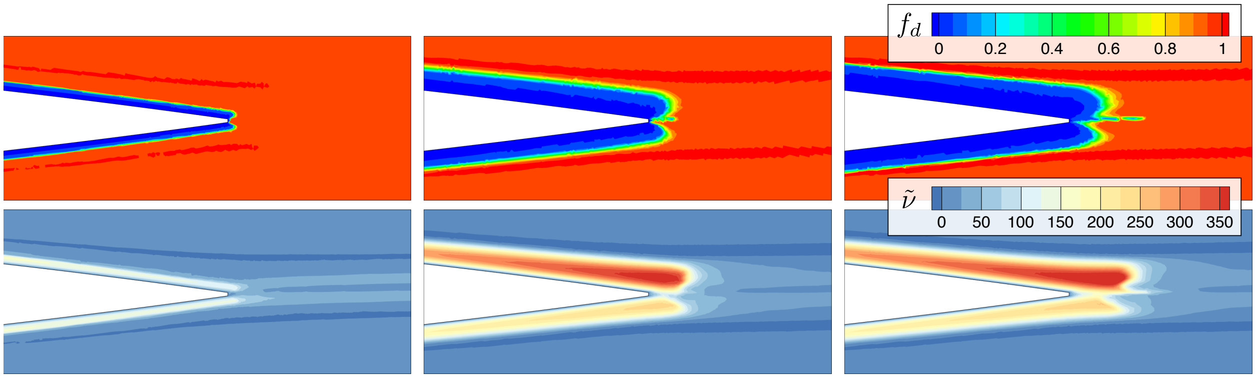

(a) $C_1 = 8$ (b) $C_1 = 16$ (c) $C_1 = 32$

Fig. 7 Contours of the shielding function (top) and the turbulence working variable (bottom) with increased shielding strength for DDES-STD using $C_{\mathrm{DES}} = 0.65$ on the 196.7K-point grid.

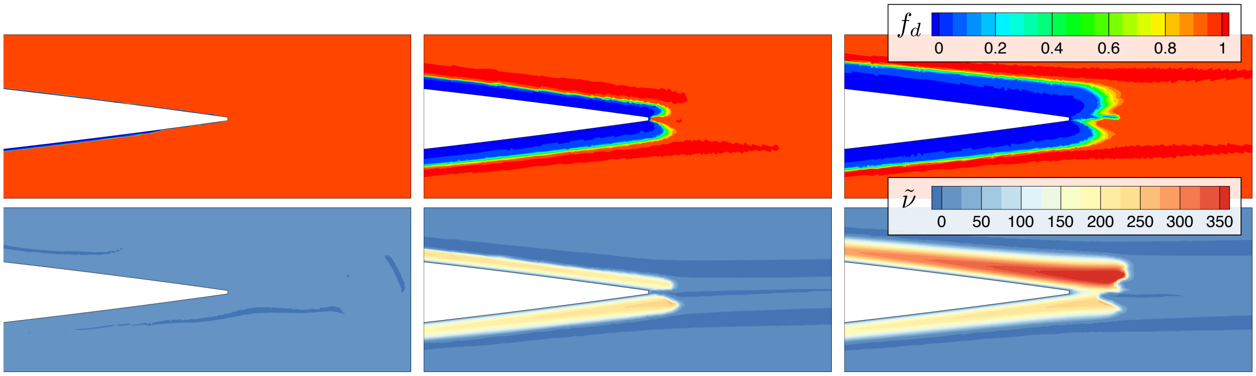

(a) $C_1 = 8$ (b) $C_1 = 16$ (c) $C_1 = 32$

Fig. 8 Contours of the shielding function (top) and the turbulence working variable (bottom) with increased shielding strength for DDES-STD using $C_{\mathrm{DES}} = 0.2$ on the 196.7K-point grid.

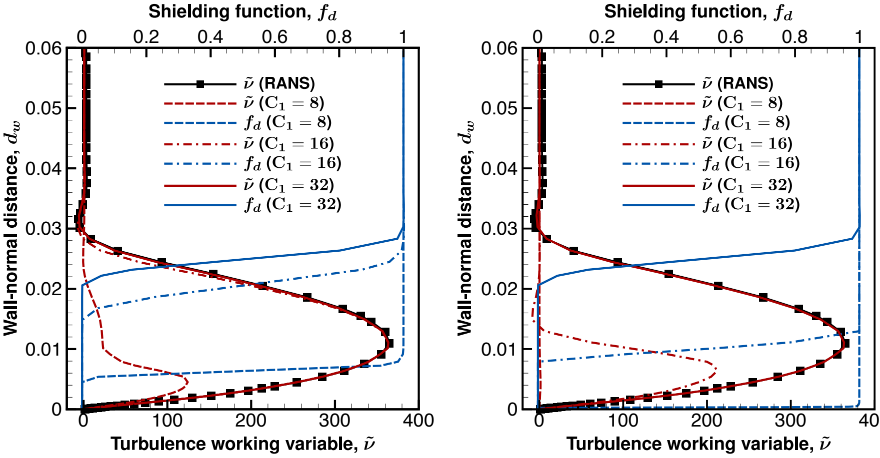

(a) $C_{\mathrm{DES}} = 0.65$ (b) $C_{\mathrm{DES}} = 0.2$

Fig. 9 Wall-normal profiles of the turbulence working variable and shielding function above the airfoil at $x = 0.98c$ computed with RANS and DDES-STD on the 196.7K-point grid, shown for increasing shielding-strength coefficients.

protection. It is also important to note that a smaller C_{DES} coefficient produces a sharper decay of $\tilde{\nu}$ when the model switches from RANS to LES. This is most easily seen by comparing the $\tilde{\nu}$ contours in the wake given in Figs. 7(c) and 8(c). Although $C_{\mathrm{DES}} = 0.2$ provides a steeper cutoff, the large C_1 coefficient still permits the RANS region to penetrate significantly into the wake, where rapid RLT is desired.

The profiles of $\tilde{\nu}$ and f_d at $x = 0.98c$ for various values of C_1 and C_{DES} on the 196.7K-point grid are shown in Fig. 9. In Fig. 9(a), increasing C_1 shifts the shielding function toward unity closer to the edge of the boundary layer compared to the standard value. This shift results in closer agreement with the RANS $\tilde{\nu}$ profile. Figure 9(b) demonstrates that for $C_1 = 8$ and $C_{\mathrm{DES}} = 0.2$, the shielding collapses entirely, resulting in imperceptibly small $\tilde{\nu}$ throughout the boundary layer. Furthermore, Fig. 9(b) confirms that even $C_1 = 16$ is insufficient to properly shield the boundary layer at this reduced value of C_{DES}. Recall that a primary adverse effect of MSD involves the underprediction of skin friction and potentially GIS. Mach contours shown in Fig. 10 obtained with the default shielding strength show the presence of GIS near the trailing edge when $C_{\mathrm{DES}} = 0.2$.

These results motivate the need for DDES-5 to provide more robust shielding without excessively smearing the grey area and delaying RLT. As has been shown, a value of C_1 significantly larger than the DDES-STD default is required to ensure strong protection of attached boundary layers for fine grids and reduced C_{DES}. For DDES-5, a default value of $C_1 = 50$ is chosen to provide conservative RANS protection in attached regions, while relying on the suppression procedure to limit the shielding locally when detached flow is detected. This capability is demonstrated in Fig. 11, which

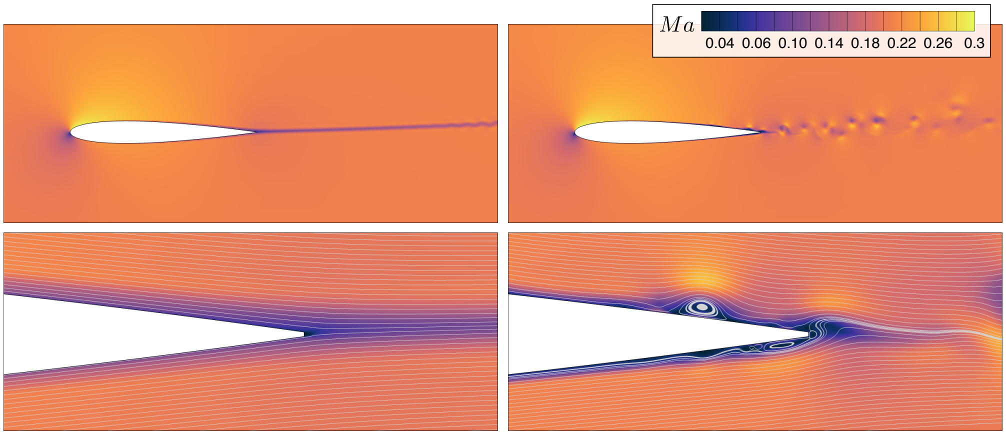

(a) $C_{\mathrm{DES}} = 0.65$ (b) $C_{\mathrm{DES}} = 0.2$

Fig. 10 Mach contours for DDES-STD with $C_1 = 8$ and varying C_{DES}.

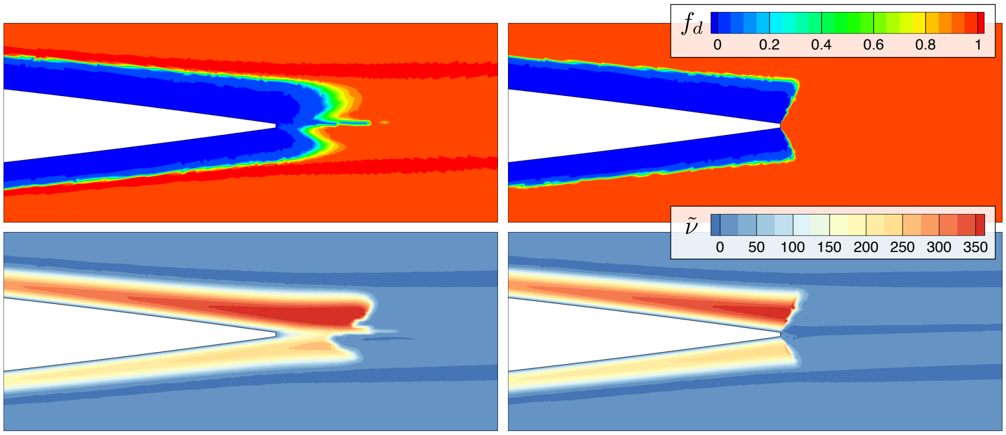

(a) DDES-STD (b) DDES-5

Fig. 11 Contours of the shielding function (top) and turbulence working variable (bottom) for DDES-STD and DDES-5, both obtained with $C_1 = 50$ and $C_{\mathrm{DES}} = 0.2$.

compares the f_d and $\tilde{\nu}$ contours computed with $C_1 = 50$ for both DDES-STD and DDES-5. As expected, Fig. 11(a) shows that the large shielding coefficient used with DDES-STD pushes the RANS region significantly beyond the trailing of the airfoil where LES mode is intended. On the other hand, Fig. 11(b) demonstrates that DDES-5 sharply suppresses the shielding at the trailing edge despite the substantial shielding coefficient.

Contours of $\tilde{\nu}$ computed with RANS and DDES-5 on the three different grids with both $C_{\mathrm{DES}} = 0.65$ and 0.2 are shown in Fig. 12. When compared with the DDES-STD results in Fig. 5, DDES-5 provides much closer agreement to RANS up to the trailing edge for all cases. With $C_{\mathrm{DES}} = 0.65$ (Figs. 12(d)-(f)), the transition to LES in the wake is more apparent with finer grid resolution, as the smaller filter width is fed into the destruction term via the DES limiter (see Eqs. 11 and 16). Figures 12(g)-(i) show a similar trend with $C_{\mathrm{DES}} = 0.2$; however, a much sharper reduction in $\tilde{\nu}$ is observed for all grids. The corresponding DDES-5 profiles above the airfoil at $x = 0.98c$ for $C_{\mathrm{DES}} = 0.65$ are plotted in

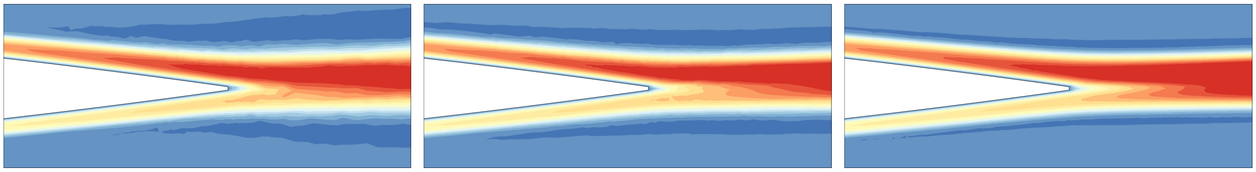

(a) RANS (34.1K) (b) RANS (75.9K) (c) RANS (196.7K)

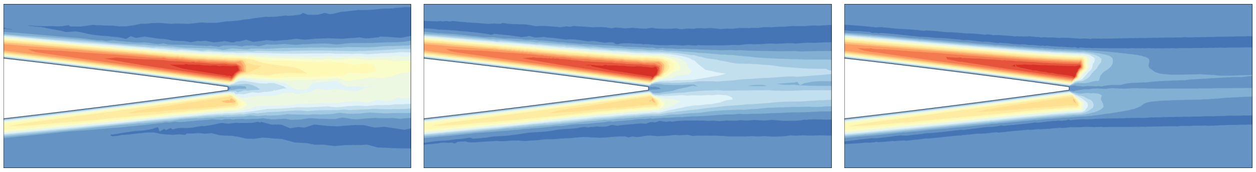

(d) DDES-5, $C_{\mathrm{DES}} = 0.65$ (34.1K) (e) DDES-5, $C_{\mathrm{DES}} = 0.65$ (75.9K) (f) DDES-5, $C_{\mathrm{DES}} = 0.65$ (196.7K)

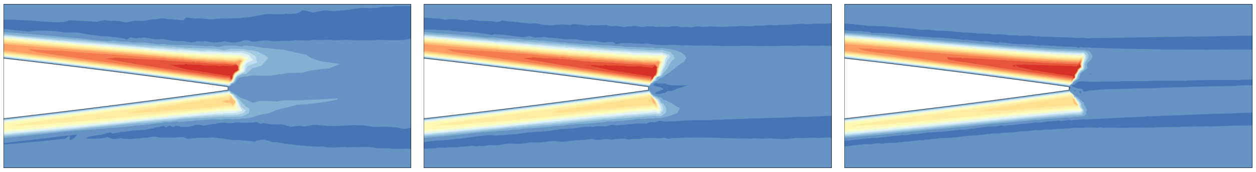

(g) DDES-5, $C_{\mathrm{DES}} = 0.2$ (34.1K) (h) DDES-5, $C_{\mathrm{DES}} = 0.2$ (75.9K) (i) DDES-5, $C_{\mathrm{DES}} = 0.2$ (196.7K)

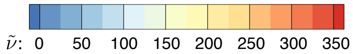

Fig. 12 Contours of the turbulence working variable obtained with RANS and DDES-5 on each grid with varying C_{DES}. Numbers in parentheses are mesh node counts in thousands.

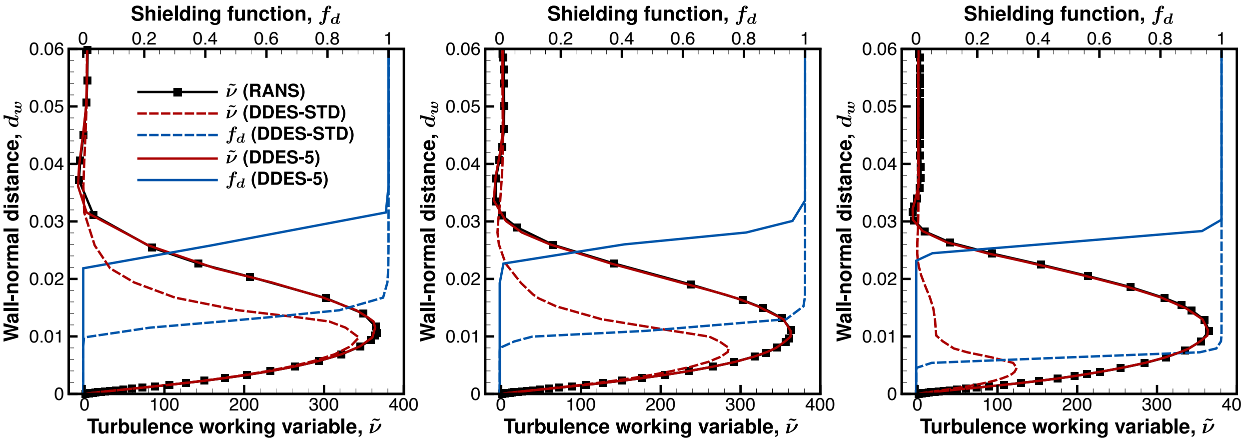

(a) Coarse grid (b) Medium grid (c) Fine grid

Fig. 13 Wall-normal profiles of the turbulence working variable and shielding function above the airfoil at $x = 0.98c$ computed with RANS, DDES-STD, and DDES-5 using $C_{\mathrm{DES}} = 0.65$.

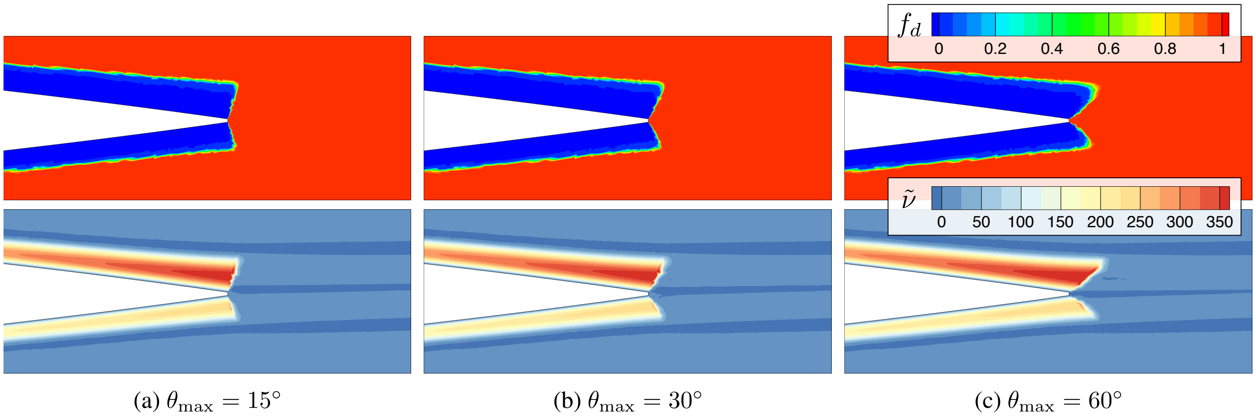

(a) $\theta_{\max} = 15°$ (b) $\theta_{\max} = 30°$ (c) $\theta_{\max} = 60°$

Fig. 14 Contours of the shielding function (top) and turbulence working variable (bottom) for DDES-5 with varying θ_{max} inputs. Note that these results are obtained with C_{DES} = 0.2.

Fig. 13 for the three different grids, along with the RANS and DDES-STD (C_1 = 8) results for comparison. Clearly, the stronger shielding coefficient used in DDES-5 maintains the same LES transition location (where f_d goes to one) for all grids, whereas the DDES-STD shielding breaks down and its transition shifts closer to the wall with increasing grid refinement. As a result, DDES-5 produces a $\tilde{\nu}$ profile that closely matches RANS for all three grids.

Beyond C_1 and C_{DES}, the only additional input parameters required by DDES-5 are θ_{min} and θ_{max}, which by default are set to 5° and 30°, respectively. As described in Sec. II.C, the DDES-5 shielding-suppression function β is more sensitive to θ_{max} than it is to θ_{min}. The resulting f_d and $\tilde{\nu}$ contours for θ_{max} = 15°, 30°, and 60° are shown in Fig. 14. Clearly, a small θ_{max} input aggressively suppresses the shielding, keeping the RLT location very close to the trailing edge. Conversely, a large θ_{max} does so more conservatively, preserving the RANS shielding a small distance past the trailing edge. In practice, it has been determined that θ_{max} = 30° provides a good balance between strong RANS protection and rapid RLT, although results ranging from θ_{max} = 15° to θ_{max} = 60° exhibit only moderate differences.

B. High-Lift Common Research Model

The purpose of the Fifth NASA/AIAA High-Lift Prediction Workshop was to assess progress towards flow prediction of aircraft configurations operating near maximum lift [1]. Here, a series of test cases was identified ranging in complexity from a simple wing-body to a full aircraft including flaps, slats, and nacelle (with strake), as well as all support structures such as flap and slat brackets and engine pylon. Participants submitted simulation results obtained from a range of physical models that include RANS, WMLES, and HRLES. Results obtained using DDES-5 are presented below for Case 1, which corresponds to a simple wing-body configuration at a single angle of attack, and for Case 2.4, which is a full high-lift configuration simulated over a range of angles of attack. All simulations are performed on the full-scale, semi-span CRM-HL.

1. HLPW-5 Case 1

The first simulation represents Case 1 from HLPW-5. The geometry is a simple wing-body at a freestream Mach number, Reynolds number, and angle of attack of $M_\infty = 0.2$, $R_e = 5.6 \times 10^6$, and $\alpha = 11°$, respectively. The objective of the test case is to repeat the simulation on a series of increasingly finer meshes to derive grid-converged solutions. Several participants submitted HRLES results for this case using slight variations of DDES. Figure 15 shows a summary of results digitized from Ref. [48]. In this work, DDES simulations are identified solely by the type of shielding employed. Consequently, any simulation that applies the standard shielding formulations and coefficients is labeled as DDES-STD, regardless of the underlying RANS model or specific variant used. For additional details on the submitted results, refer to Ref. [48]. As seen in the figure, the computed lift results obtained with DDES using the standing shielding formulation initially exhibit increasing lift between the coarsest and next-coarsest meshes, but ultimately display a dramatic reduction in lift as the mesh is refined. This drop has been attributed to MSD caused by inadequate shielding of the boundary layer. Conversely, results obtained using the shielding functions described in Refs. [32] (DDES-DR/dark blue) and [26] (DDES-SBES/green) do not exhibit the sharp drop in lift as observed using the DDES-STD approach, which indicates that the boundary layer is much better protected with mesh refinement. FUN3D finite-volume results

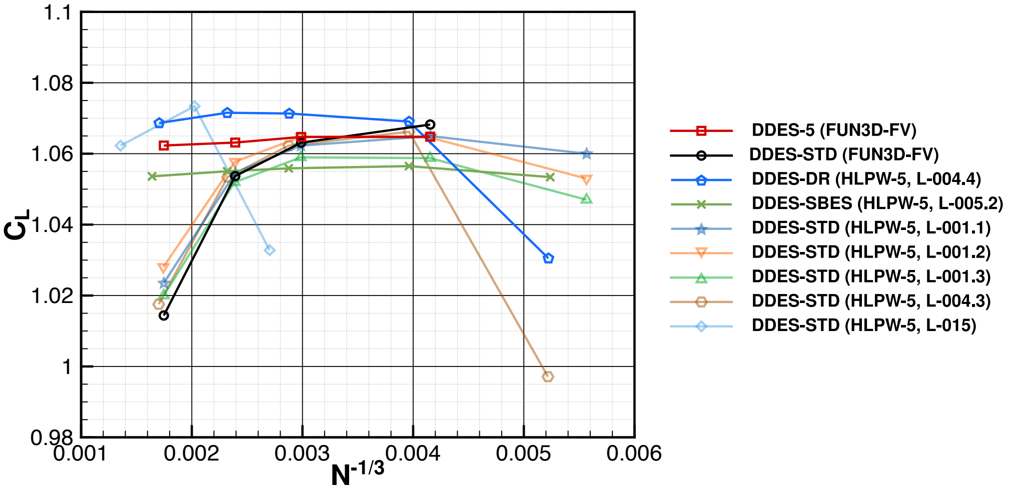

Fig. 15 Grid convergence study of the lift coefficient obtained with DDES-STD and DDES-5 compared with HLPW-5 results for Case 1.

obtained using DDES-5 are also included on the same figure (DDES-5/red). These results have been computed on meshes ranging in size from approximately 14 million grid points up to 187.5 million grid points. As shown in the figure, the lift remains relatively stable as the mesh is refined, which suggests that MSD is not present. This contrasts with the results obtained using standard DDES shielding, where a sharp drop in lift is observed. Note that the final lift values for the three results that do not show evidence of MSD are within approximately 1.4% of each other, with the differences likely attributable to the distinct turbulence models used in each simulation.

2. HLPW-5 Case 2.4

Test Case 2 of HLPW-5 features a configuration-buildup study designed to assess aerodynamic predictions across increasingly complex versions of the CRM-HL. Each successive configuration introduces additional geometric detail, building incrementally on the previous one. This work presents results specifically for Case 2.4, which is the full landing configuration with all high-lift devices installed. This geometry includes the fuselage, leading-edge slats, slat brackets, main wing, trailing-edge flaps, flap fairings, horizontal and vertical tails, nacelle pylon, and flow-through nacelle with a

Fig. 16 NASA CRM-HL surface mesh near the nacelle for Case 2.4 (114M-point grid).

chine as a vortex generator. Flow over this CRM-HL configuration is computed for a range of angles of attack extending beyond maximum lift. The freestream Mach and Reynolds numbers are 0.2 and $R_e = 5.9 \times 10^6$.

DDES-5 computations are performed with FUN3D-FE on a grid with 114 million points and with FUN3D-FV on a grid with 220 million points. A coarser grid is used with FUN3D-FE because it is more computationally expensive than FUN3D-FV but requires less grid points to achieve a similar level of accuracy. The normal spacing at the wall is set such that $\Delta y_w^+ = 1$ and $\Delta y_w^+ = 0.5$ for the 114M-point grid and the 220M-point grid, respectively, based on a flat-plate approximation using the freestream conditions. It should be emphasized that, in general, DDES meshes are not typical RANS meshes but instead require finer wall-parallel spacing so that the LES regions, whose locations are not known prior to the simulation, can be adequately resolved. This is illustrated in Fig. 16, which shows a portion of the surface mesh for the 114M-point grid with fine streamwise and spanwise spacing covering the entire geometry. To evaluate how DDES-5 compares with WMLES for Case 2.4, FUN3D-FV WMLES results on a grid with 419 million points are included, which were obtained in Ref. [4]. The computational results are validated against experimental measurements for the 5.1% full-span model obtained in the ONERA F1 wind tunnel [49].

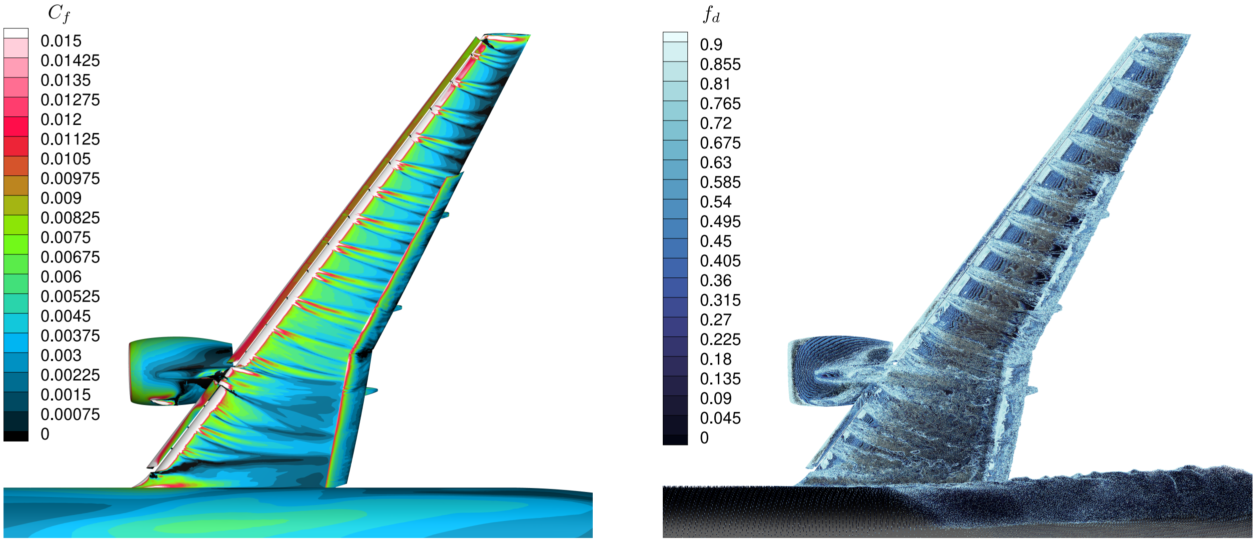

(a) Skin friction (planform view)

(b) Shielding function (planform view)

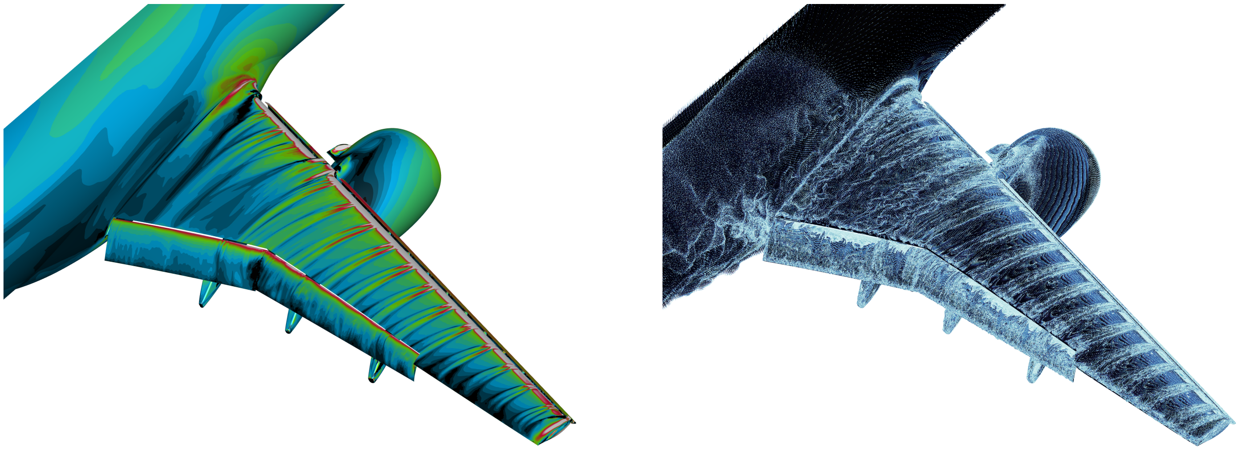

(c) Skin friction (3D view)

(d) Shielding function (3D view)

Fig. 17 Instantaneous skin friction and near-wall shielding at $\alpha = 19.7°$ for DDES-5 (FUN3D-FE) on the 114M-point grid.

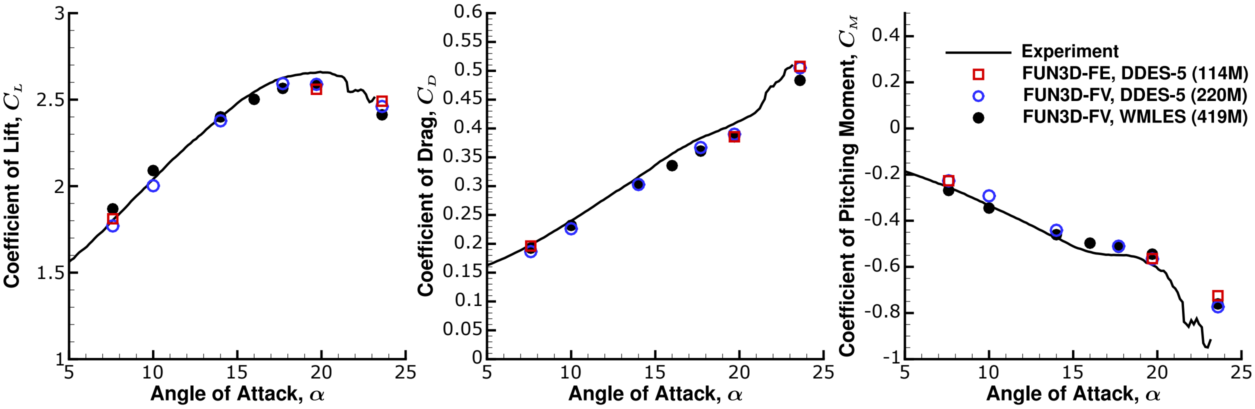

(a) C_L (b) C_D (c) C_M

Fig. 18 Force and moment polars obtained with DDES-5 and WMLES for HLPW-5 Case 2.4.

Computations with FUN3D-FV (both DDES-5 and WMLES) were performed at the following angles of attack: α = 7.6°, 10°, 14°, 17.7°, 19.7°, and 23.6° (WMLES additionally includes 16°). Due to computing-resource constraints, FUN3D-FE was run only at α = 7.6°, 19.7°, and 23.6°.

Surface contours of the instantaneous skin friction coefficient computed by FUN3D-FE with DDES-5 on the 114M-point grid at 19.7° angle of attack are shown on the left-hand side of Fig. 17. This figure demonstrates that DDES-5 avoids the large, triangular separation patterns on the upper wing surface outboard of the flap that are commonly observed in pure RANS simulations [50]. These nonphysical separation patterns originate from the inability of RANS to accurately model the detached slat bracket wakes near the leading edge of the main wing element. Although DDES relies on an underlying RANS model, its eddy-resolving capability sufficiently captures the turbulent dynamics in the slat wakes, thereby preventing the separation defect that RANS exhibits at high angles of attack. Scatter plots of the cell-averaged shielding function values near the wall are shown on the right-hand side of Fig. 17. To improve visibility of the near-wall data, points with f_d values greater than 0.9 are omitted, as these correspond to regions farther from the wall where the flow is in pure LES mode (f_d = 1) and would otherwise obscure the view. The darker regions indicate attached RANS treatment, while the lighter areas show where the model is transitioning to LES. Notably, shielding is suppressed (i.e., higher f_d) in the slat wakes near the leading edge of the main wing, suggesting the presence of resolved turbulence via LES, which is evidently critical for preventing the spurious separation wedges common to RANS.

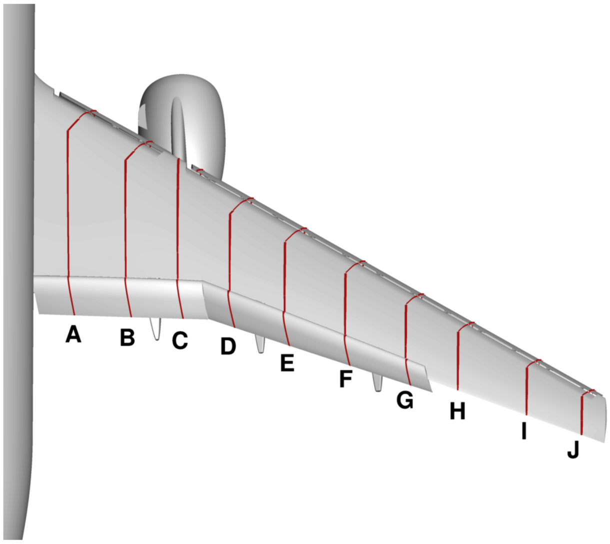

Fig. 19 Station locations for surface-pressure measurements used for both experiments and computations.

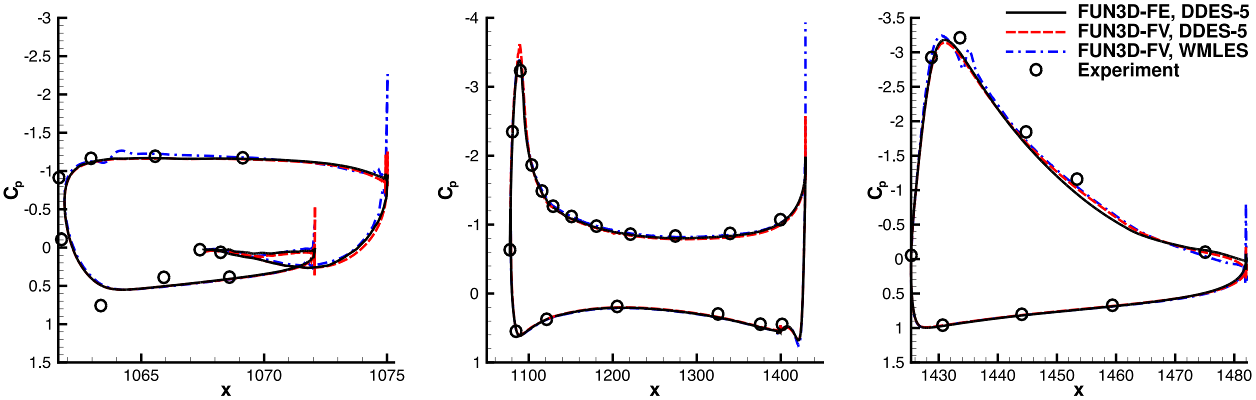

(a) Station A

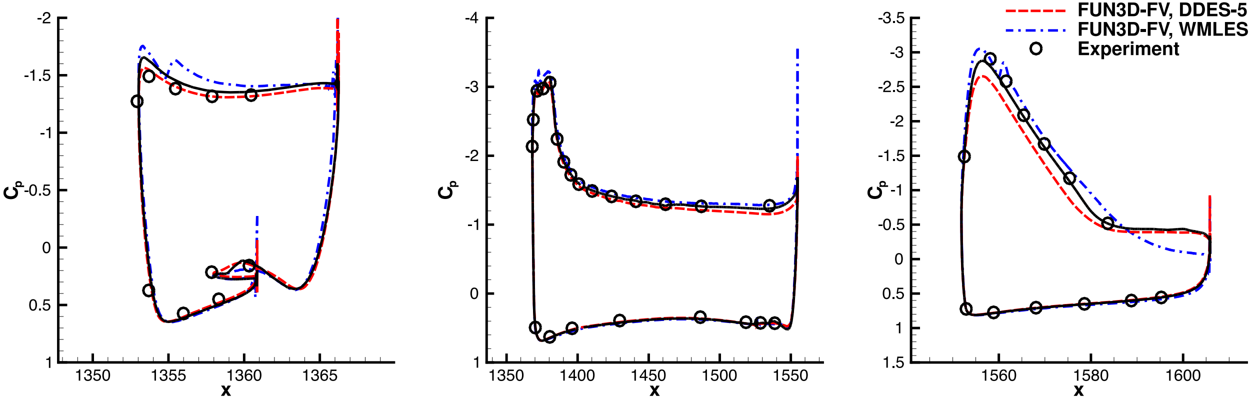

(b) Station E

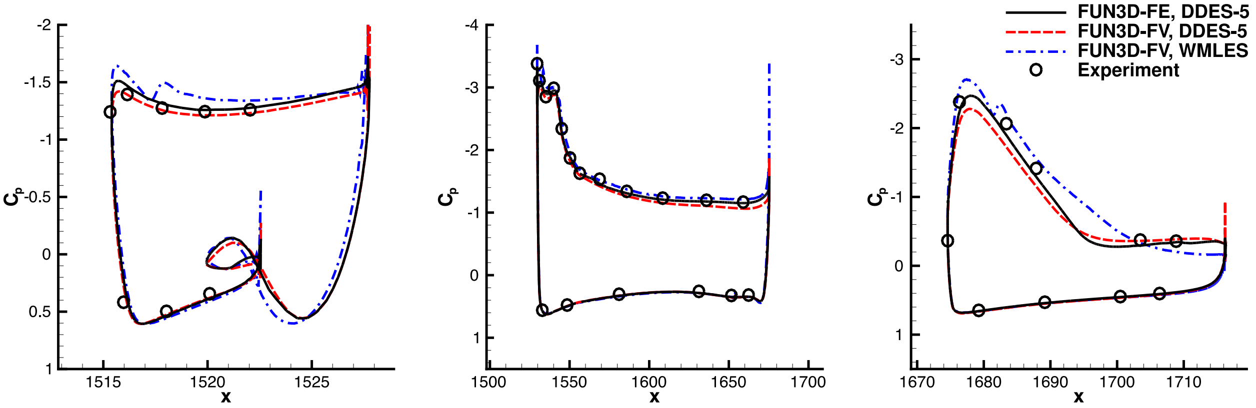

(c) Station G

Fig. 20 Surface-pressure distributions at three spanwise stations along the slat (left), main wing (center), and flap (right) for $\alpha = 7.6°$.

Lift, drag, and pitching moment polars for DDES-5, WMLES, and experiments are shown in Fig. 18, spanning the linear, maximum-lift, and post-stall regimes. In general, all computed results show reasonable agreement with one another and with experiments. In Fig. 18(a), which presents the lift coefficient versus angle of attack, WMLES overpredicts lift at low angles of attack ($\alpha = 7.6°$ and 10°), whereas both DDES-5 solutions align closer with the experimental data. Near maximum-lift ($\alpha = 19.7°$), all computations slightly underpredict $C_{L,max}$; however, the critical angle of attack where $C_{L,max}$ occurs is well predicted in all cases. For the post-stall cases ($\alpha = 23.6°$), both DDES-5 solutions yield lift coefficients closer to the experimental data than WMLES. From Fig. 18(b), all computed drag polars agree closely with one another and with the experimental trend, though they show a slight downward offset

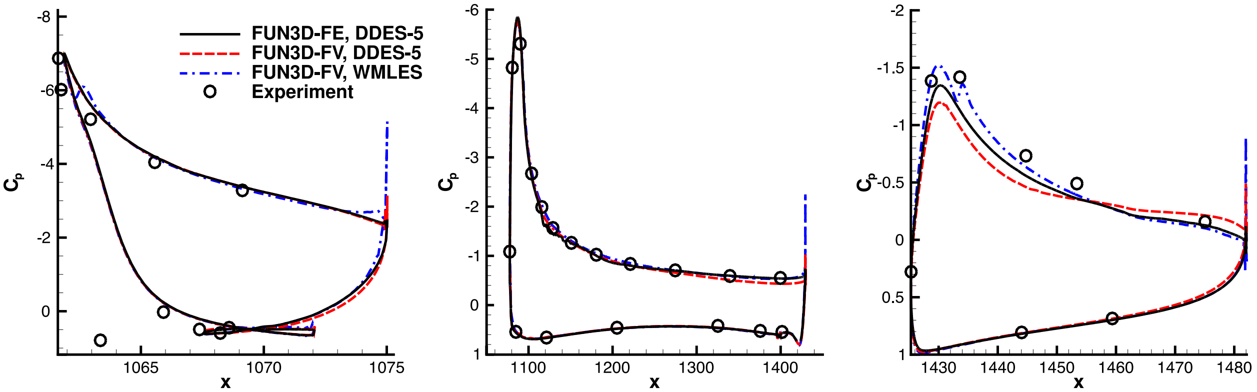

(a) Station A

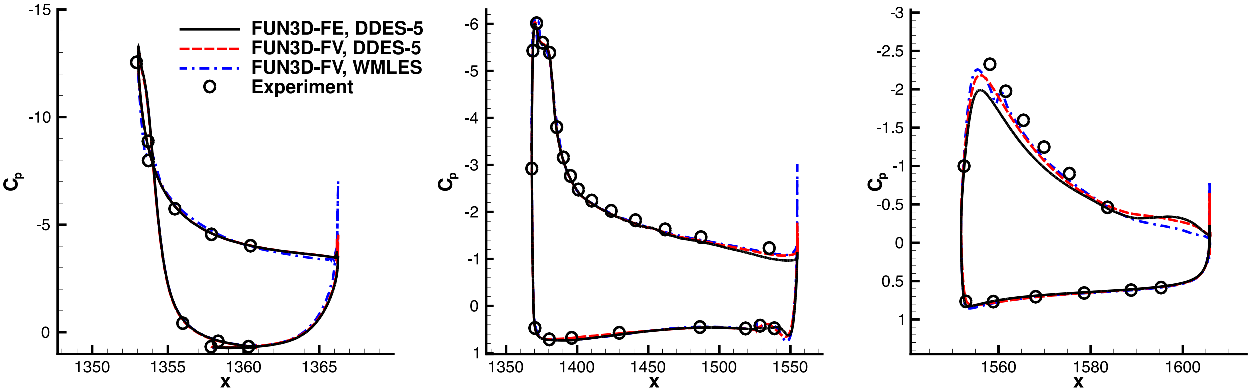

(b) Station E

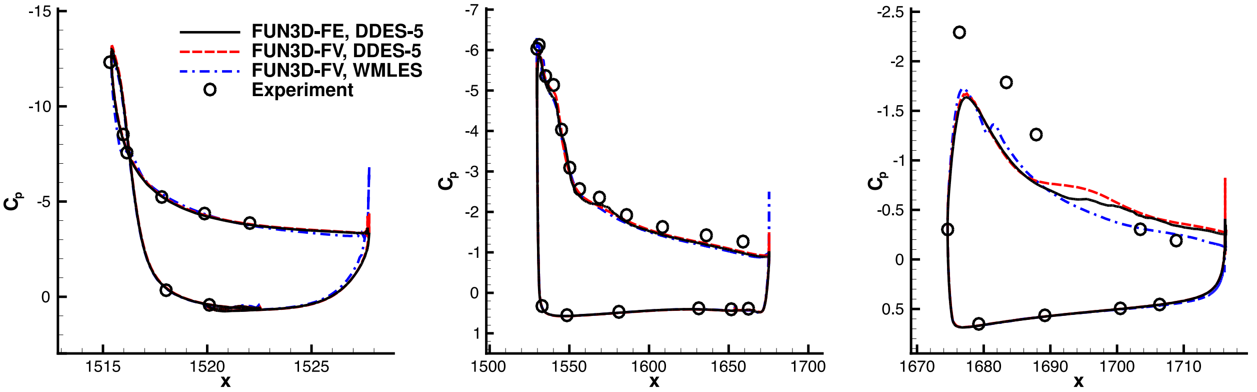

(c) Station G

Fig. 21 Surface-pressure distributions at three spanwise stations along the slat (left), main wing (center), and flap (right) for α = 19.7°.

from experiments across all angles of attack. The post-stall drag obtained by both DDES-5 simulations is closer to the experiment than that predicted by WMLES. Figure 18(c) shows good agreement between the simulated and experimental pitching moment coefficients up to stall, after which the moment is less negative in all simulations than in the experiment.

Figures 20, 21, and 22 give time-averaged surface-pressure distributions obtained from simulations and experiments for α = 7.6°, 19.7°, and 23.6°, respectively. The corresponding station locations are given in Fig. 19. The simulated pressure coefficients for α = 7.6° in Fig. 20 show good overall agreement with the experiment. WMLES slightly overpredicts the suction on the slat at Stations E and G, whereas both DDES-5 results lie closer to the experimental pressure coefficients. A fairly large deviation in the DDES-5 and WMLES simulations can be seen on the flap along

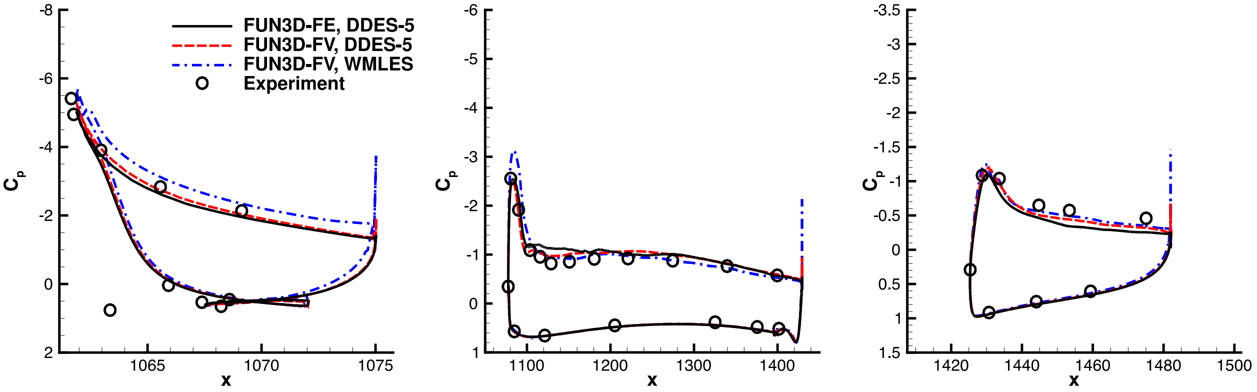

(a) Station A

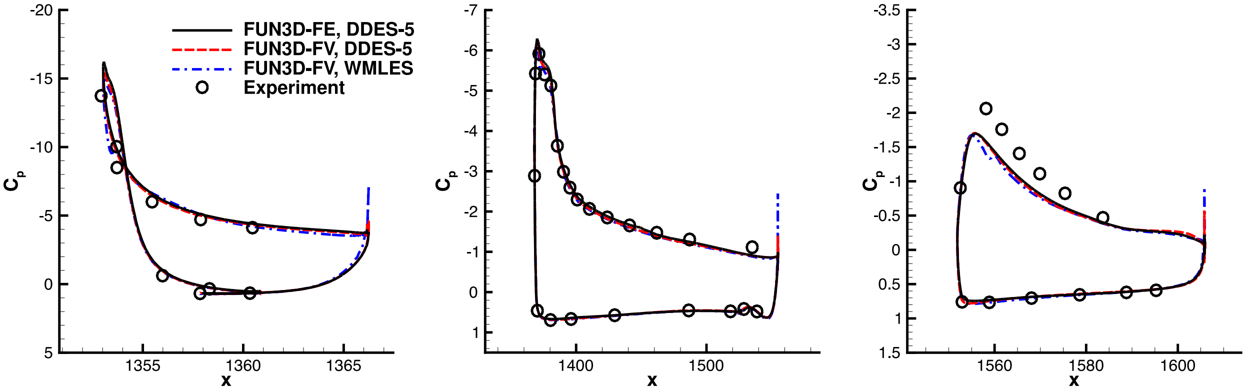

(b) Station E

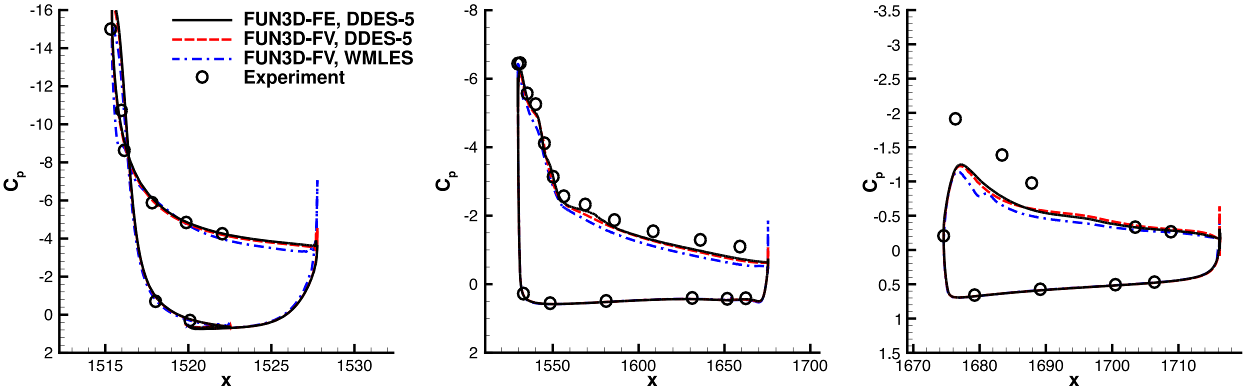

(c) Station G

Fig. 22 Surface-pressure distributions at three spanwise stations along the slat (left), main wing (center), and flap (right) for $\alpha = 23.6°$.

Stations E and G. Experimental oil flow visualizations (see Ref. [4]) confirm substantial trailing-edge separation across the outboard flap. DDES-5 successfully predicts the extent of flap trailing-edge separation, while WMLES does not. Both of these effects contribute to the overpredicted integrated lift computed by WMLES at $\alpha = 7.6$, as shown in Fig. 18(a). Although the two DDES-5 pressure distributions are mostly consistent, FUN3D-FV yields slightly reduced suction relative to FUN3D-FE and WMLES, particularly on the flaps at Stations E and G before separation.

The simulations at $\alpha = 19.7°$ and $23.6°$ also broadly reproduce the experimental pressure coefficients with high fidelity, except for a notable underprediction of the suction peak on the outboard flap at Stations E and G for both angles of attack. Furthermore, all three simulations predict slightly weaker suction on the main wing at Station G for both α = 19.7° and 23.6°. These underpredictions in negative pressure account for the lower integrated lift values observed in the high-angle-of-attack cases. The reduced negative pressure computed on the aft wing and flap contribute a more nose-up pitching moment, which explains the milder pitch break predicted by the simulations compared to the experiment, as shown in Fig. 18(c). Both DDES-5 and WMLES produce similar pressure distributions at the higher angles of attack, aside from a few noteworthy distinctions. At α = 19.7°, WMLES better captures the suction peak on the inboard flap (Station A) than either DDES-5 result, with FUN3D-FE performing incrementally better than FUN3D-FV. At Station E for the same α, the flap suction peaks predicted by FUN3D-FV DDES-5 and WMLES are quite similar, both aligning closer to the experiment than the FUN3D-FE prediction.

V. Conclusions

A straightforward modification to the standard DDES shielding technique was introduced that rectifies the MSD and slow RLT issues common with the original approach. The proposed method, termed DDES-5, permits universal strengthening of the shielding function to better protect attached boundary layers while employing an additional function that locally suppresses the shielding when separated or detached flow is detected. The new suppression function considers the alignment of the local velocity vector and a wall-parallel vector, obtained from the gradient of the wall-normal distance field. For an attached boundary layer, these vectors are well-aligned, and the DDES model should provide strong RANS coverage over the entire boundary layer. Otherwise, the flow is likely detached, and the suppression function ramps down the shielding and allows for LES treatment to prevail. The approach is entirely local, easy to implement, and requires little to no calibration.

Before presenting results with the method, numerical dissipation was studied with the inviscid Taylor-Green vortex, suggesting the use of a smaller coefficient controlling the SGS dissipation (C_{DES}), which has implications for MSD and RLT. The DDES-5 method was then evaluated for a simple attached flow over a NACA 0012 airfoil. A core principle of the original DDES formulation is that the entire attached boundary layer should be modeled using RANS. Accordingly, this test case aimed to verify that DDES-5 can accurately reproduce the RANS solution along the full chord where the flow remains attached. Initially, the presence of MSD was demonstrated using the original DDES shielding function across progressively refined grids. While increasing the shielding coefficients was shown to mitigate MSD, it also undesirably extended the RLT region, delaying the onset of LES content in separated flow areas. DDES-5 was shown to remedy this delay in RLT while providing robust RANS shielding over the entire airfoil.

The capability of DDES-5 was then evaluated on more complex flow cases from the HLPW-5 involving the NASA CRM-HL configuration. First, a grid convergence study was performed on the simple wing-body configuration (Case 1) using DDES-5 with the FUN3D-FV solver. All workshop submissions for this case that used the standard DDES shielding function exhibited a significant loss of lift on the high-resolution grids due to MSD, whereas DDES-5 demonstrated far greater resistance to this defect. Next, an angle-of-attack sweep for the CRM-HL in full-landing configuration (Case 2.4) was performed using DDES-5 with FUN3D-FE on a 112M-point grid and FUN3D-FV on 240M-point grid. Both DDES-5 results revealed close agreement with experimental wind-tunnel data. Furthermore, the DDES-5 simulations predicted flap separation at lower angles of attack, whereas FUN3D-FV WMLES on a 419M-point did not capture the extent of the separation and consequently overpredicted lift at low angles compared to the experimental data.

Acknowledgments

This work is supported by the NASA Transformational Tools and Technologies (TTT) project of the Transformative Aeronautics Concepts Program (TACP) under the Aeronautics Research Mission Directorate (ARMD). The authors would like to thank Dr. Philippe Spalart for his valuable guidance and for the insightful discussions related to this work.

References

[1] Clark, A. M., Rumsey, C. L., Slotnick, J. P., and Wang, L., "High-Lift Prediction Workshop 5: Overview and Workshop Summary," *AIAA SCITECH 2025 Forum*, American Institute of Aeronautics and Astronautics, Orlando, FL, 2025. https://doi.org/10.2514/6.2025-0045.

[2] Slotnick, J., Khodadoust, A., Alonso, J., Darmofal, D., Gropp, W., Lurie, E., and Mavriplis, D., "CFD Vision 2030 Study: A Path to Revolutionary Computational Aerosciences," Tech. Rep. NASA/CR–2014-218178, Mar. 2014. URL https://ntrs.nasa.gov/citations/20140003093.

[3] Kawai, S., and Larsson, J., "Wall-Modeling in Large Eddy Simulation: Length Scales, Grid Resolution, and Accuracy," *Physics of Fluids*, Vol. 24, No. 1, 2012, p. 015105. https://doi.org/10.1063/1.3678331.

[4] Wang, L., Rumsey, C. L., Anderson, W. K., Nielsen, E. J., Iyer, P. S., Wick, A., Walden, A., Nastac, G., and Diskin, B., "WMLES for the Fifth High-Lift Prediction Workshop Cases Using FUN3D," *AIAA SCITECH 2025 Forum*, American Institute of Aeronautics and Astronautics, Orlando, FL, 2025. https://doi.org/10.2514/6.2025-1079.

[5] Spalart, P. R., "Comments on the Feasibility of LES for Wings and on the Hybrid RANS/LES Approach," *Proceedings of the First AFOSR International Conference on DNS/LES*, 1997, pp. 137–147.

[6] Mockett, C., "A Comprehensive Study of Detached-Eddy Simulation," Ph.D. thesis, Technische Universität Berlin, Berlin, 2009. https://doi.org/10.14279/depositonce-2305.

[7] Spalart, P. R., and Allmaras, S. R., "A One-Equation Turbulence Model for Aerodynamic Flows," *30th Aerospace Sciences Meeting and Exhibit*, American Institute of Aeronautics and Astronautics, Reno, NV, U.S.A., 1992. https://doi.org/10.2514/6.1992-439.

[8] Menter, F. R., "Two-Equation Eddy-Viscosity Turbulence Models for Engineering Applications," *AIAA Journal*, Vol. 32, No. 8, 1994, pp. 1598–1605. https://doi.org/10.2514/3.12149.

[9] Travin, A., Shur, M., Strelets, M., and Spalart, P. R., "Physical and Numerical Upgrades in the Detached-Eddy Simulation of Complex Turbulent Flows," *Advances in LES of Complex Flows*, Vol. 65, edited by R. Moreau, R. Friedrich, and W. Rodi, Springer Netherlands, Dordrecht, 2002, pp. 239–254. https://doi.org/10.1007/0-306-48383-1_16, series Title: Fluid Mechanics and Its Applications.

[10] Strelets, M., "Detached Eddy Simulation of Massively Separated Flows," *39th Aerospace Sciences Meeting and Exhibit*, American Institute of Aeronautics and Astronautics, Reno, NV, U.S.A., 2001. https://doi.org/10.2514/6.2001-879.

[11] Menter, F. R., and Kuntz, M., "Adaptation of Eddy-Viscosity Turbulence Models to Unsteady Separated Flow Behind Vehicles," *The Aerodynamics of Heavy Vehicles: Trucks, Buses, and Trains*, Vol. 19, edited by F. Pfeiffer, P. Wriggers, R. McCallen, F. Browand, and J. Ross, Springer Berlin Heidelberg, Berlin, Heidelberg, 2004, pp. 339–352. https://doi.org/10.1007/978-3-540-44419-0_30, series Title: Lecture Notes in Applied and Computational Mechanics.

[12] Spalart, P. R., Deck, S., Shur, M. L., Squires, K. D., Strelets, M. K., and Travin, A., "A New Version of Detached-eddy Simulation, Resistant to Ambiguous Grid Densities," *Theoretical and Computational Fluid Dynamics*, Vol. 20, No. 3, 2006, pp. 181–195. https://doi.org/10.1007/s00162-006-0015-0.

[13] Probst, A., Wolf, C., Radespiel, R., Knopp, T., Schwamborn, D., and Radespiel, R., "A Comparison of Detached-Eddy Simulation and Reynolds-Stress Modeling Applied to the Flow over a Backward-Facing Step and an Airfoil at Stall," *48th AIAA Aerospace Sciences Meeting Including the New Horizons Forum and Aerospace Exposition*, American Institute of Aeronautics and Astronautics, Orlando, Florida, 2010. https://doi.org/10.2514/6.2010-920.

[14] Ashton, N., West, A., and Mendonça, F., "Flow Dynamics Past a 30P30N Three-Element Airfoil Using Improved Delayed Detached-Eddy Simulation," *AIAA Journal*, Vol. 54, No. 11, 2016, pp. 3657–3667. https://doi.org/10.2514/1.J054521.

[15] Ashton, N., "Recalibrating Delayed Detached-Eddy Simulation to eliminate modelled-stress depletion," *23rd AIAA Computational Fluid Dynamics Conference*, American Institute of Aeronautics and Astronautics, Denver, Colorado, 2017. https://doi.org/10.2514/6.2017-4281.

[16] Gritskevich, M. S., Garbaruk, A. V., Schütze, J., and Menter, F. R., "Development of DDES and IDDES Formulations for the k-ω Shear Stress Transport Model," *Flow, Turbulence and Combustion*, Vol. 88, No. 3, 2012, pp. 431–449. https://doi.org/10.1007/s10494-011-9378-4.

[17] Siggeirsson, E. M., Andersson, N., and Wallin, F., "Sensitivity Study of the SA-DDES Shielding Function," *2018 AIAA Aerospace Sciences Meeting*, American Institute of Aeronautics and Astronautics, Kissimmee, Florida, 2018. https://doi.org/10.2514/6.2018-1355.

[18] Jain, N., and Baeder, J. D., "Assessment of Shielding Parameters in Conventional DDES Method under the Presence of Alternative Turbulence Length Scales," *23rd AIAA Computational Fluid Dynamics Conference*, American Institute of Aeronautics and Astronautics, Denver, Colorado, 2017. https://doi.org/10.2514/6.2017-4282.

[19] Mockett, C., Fuchs, M., Garbaruk, A., Shur, M., Spalart, P., Strelets, M., Thiele, F., and Travin, A., "Two Non-zonal Approaches to Accelerate RANS to LES Transition of Free Shear Layers in DES," *Progress in Hybrid RANS-LES Modelling*, Vol. 130, edited by S. Girimaji, W. Haase, S.-H. Peng, and D. Schwamborn, Springer International Publishing, Cham, 2015, pp. 187–201. https://doi.org/10.1007/978-3-319-15141-0_15, series Title: Notes on Numerical Fluid Mechanics and Multidisciplinary Design.

[20] Vatsa, V., and Lockard, D., "Assessment of Hybrid RANS/LES Turbulence Models for Aeroacoustics Applications," *16th AIAA/CEAS Aeroacoustics Conference*, American Institute of Aeronautics and Astronautics, Stockholm, Sweden, 2010. https://doi.org/10.2514/6.2010-4001.

[21] Shur, M. L., Spalart, P. R., Strelets, M. K., and Travin, A. K., "Synthetic Turbulence Generators for RANS-LES Interfaces in Zonal Simulations of Aerodynamic and Aeroacoustic Problems," *Flow, Turbulence and Combustion*, Vol. 93, No. 1, 2014, pp. 63–92. https://doi.org/10.1007/s10494-014-9534-8.

[22] Strelets, M., Shur, M., Travin, A., and Spalart, P. R., "The Delay of RANS-to-LES Transition in Hybrid RANS-LES Approaches and Some Recently Proposed Remedies," *Advances in Simulation of Wing and Nacelle Stall*, Vol. 131, edited by R. Radespiel, R. Niehuis, N. Kroll, and K. Behrends, Springer International Publishing, Cham, 2016, pp. 3–21. https://doi.org/10.1007/978-3-319-21127-5_1, series Title: Notes on Numerical Fluid Mechanics and Multidisciplinary Design.

[23] Probst, A., Radespiel, R., and Knopp, T., "Detached-Eddy Simulation of Aerodynamic Flows Using a Reynolds-Stress Background Model and Algebraic RANS/LES Sensors," *20th AIAA Computational Fluid Dynamics Conference*, American Institute of Aeronautics and Astronautics, Honolulu, Hawaii, 2011. https://doi.org/10.2514/6.2011-3206.

[24] Knopp, T., and Probst, A., "An Algebraic Sensor for the RANS-LES Switch in Delayed Detached-Eddy Simulation," *New Results in Numerical and Experimental Fluid Mechanics VIII*, Vol. 121, edited by A. Dillmann, G. Heller, H.-P. Kreplin, W. Nitsche, and I. Peltzer, Springer Berlin Heidelberg, Berlin, Heidelberg, 2013, pp. 457–464. https://doi.org/10.1007/978-3-642-35680-3_54, series Title: Notes on Numerical Fluid Mechanics and Multidisciplinary Design.

[25] He, C., Liu, Y., and Yavuzkurt, S., "A Dynamic Delayed Detached-eddy Simulation Model for Turbulent Flows," *Computers & Fluids*, Vol. 146, 2017, pp. 174–189. https://doi.org/10.1016/j.compfluid.2017.01.018.

[26] Menter, F., "Stress-Blended Eddy Simulation (SBES)—A New Paradigm in Hybrid RANS-LES Modeling," *Progress in Hybrid RANS-LES Modelling*, Vol. 137, edited by Y. Hoarau, S.-H. Peng, D. Schwamborn, and A. Revell, Springer International Publishing, Cham, 2018, pp. 27–37. https://doi.org/10.1007/978-3-319-70031-1_3, series Title: Notes on Numerical Fluid Mechanics and Multidisciplinary Design.

[27] Weihing, P., Letzgus, J., Lutz, T., and Krämer, E., "Development of Alternative Shielding Functions for Detached-Eddy Simulations," *Progress in Hybrid RANS-LES Modelling*, Vol. 143, edited by Y. Hoarau, S.-H. Peng, D. Schwamborn, A. Revell, and C. Mockett, Springer International Publishing, Cham, 2020, pp. 109–118. https://doi.org/10.1007/978-3-030-27607-2_8, series Title: Notes on Numerical Fluid Mechanics and Multidisciplinary Design.

[28] Islam, A., and Thornber, B., "A High-Order Hybrid Turbulence Model with Implicit Large-Eddy Simulation," *Computers & Fluids*, Vol. 167, 2018, pp. 292–312. https://doi.org/10.1016/j.compfluid.2018.03.031.

[29] Dong, Y., Deng, X., and Wang, G., "An Enhanced Version of Delayed Detached-Eddy Simulation Based on the $\overline{v^2} - f$ Model," *Flow, Turbulence and Combustion*, Vol. 102, No. 1, 2019, pp. 167–188. https://doi.org/10.1007/s10494-018-9957-8.

[30] Lei, D., Yang, H., Zheng, Y., Gao, Q., and Jin, X., "A Modified Shielding and Rapid Transition DDES Model for Separated Flows," *Entropy*, Vol. 25, No. 4, 2023, p. 613. https://doi.org/10.3390/e25040613.

[31] Guo, X., and Liu, J., "Protected Detached Eddy Simulation: A Model for Advanced Shielding Function Performance," *Aerospace Science and Technology*, Vol. 165, 2025, p. 110534. https://doi.org/10.1016/j.ast.2025.110534.

[32] Deck, S., and Renard, N., "Towards an Enhanced Protection of Attached Boundary Layers in Hybrid RANS/LES Methods," *Journal of Computational Physics*, Vol. 400, 2020, p. 108970. https://doi.org/10.1016/j.jcp.2019.108970.

[33] Renard, N., Vaquero, J., Gand, F., and Deck, S., "A Fully Automatic and Robust Hybrid Reynolds-Averaged Navier–Stokes/Large Eddy Simulation Approach Based on the Menter Shear Stress Transport k–ω Model," *Physics of Fluids*, Vol. 36, No. 11, 2024, p. 115160. https://doi.org/10.1063/5.0222762.

[34] Diskin, B., and Thomas, J. L., "Notes on Accuracy of Finite-Volume Discretization Schemes on Irregular Grids," *Applied Numerical Mathematics*, Vol. 60, No. 3, 2010, pp. 224–226. https://doi.org/10.1016/j.apnum.2009.12.001.

[35] Anderson, W. K., Biedron, R. T., Carlson, J.-R., Derlaga, J. M., Diskin, B., Druyor Jr., C. T., Gnoffo, P. A., Hammond, D. P., Jacobson, K. E., Jones, W. T., Kleb, B., Lee-Rausch, E. M., Liu, Y., Lohry, M. W., Nastac, G. C., Nielsen, E. J., Padway, E. M., Park, M. A., Rumsey, C. L., Thomas, J. L., Thompson, K. B., Wagner, J. J., Walden, A., Wang, L., Wood, S. L., Wood, W. A., and Zhang, X., "FUN3D Manual: 14.2," 2025. URL https://fun3d.larc.nasa.gov/papers/FUN3D_INTG_Manual-14.2.pdf.

[36] Anderson, W., and Bonhaus, D. L., "An Implicit Upwind Algorithm for Computing Turbulent Flows on Unstructured Grids," *Computers & Fluids*, Vol. 23, No. 1, 1994, pp. 1–21. https://doi.org/10.1016/0045-7930(94)90023-X.

[37] Anderson, W. K., Newman, J. C., and Karman, S. L., "Stabilized Finite Elements in FUN3D," *Journal of Aircraft*, Vol. 55, No. 2, 2018, pp. 696–714. https://doi.org/10.2514/1.C034482.

[38] Allmaras, S. R., Johnson, F. T., and Spalart, P. R., "Modifications and Clarifications for the Implementation of the Spalart-Allmaras Turbulence Model," Big Island, Hawaii, 2012, pp. ICCFD7–1902.

[39] White, F. M., and Majdalani, J., *Viscous Fluid Flow*, McGraw-Hill, New York, 2021.

[40] Rumsey, C., Smith, B., and Huang, G., "Description of a Website Resource for Turbulence Modeling Verification and Validation," *40th Fluid Dynamics Conference and Exhibit*, American Institute of Aeronautics and Astronautics, Chicago, Illinois, 2010. https://doi.org/10.2514/6.2010-4742.

[41] Vatsa, V. N., Lockard, D. P., and Spalart, P. R., "Grid Sensitivity of SA-Based Delayed-Detached-Eddy-Simulation Model for Blunt-Body Flows," *AIAA Journal*, Vol. 55, No. 8, 2017, pp. 2842–2847. https://doi.org/10.2514/1.J055685.

[42] Roe, P., "Approximate Riemann Solvers, Parameter Vectors, and Difference Schemes," *Journal of Computational Physics*, Vol. 43, No. 2, 1981, pp. 357–372. https://doi.org/10.1016/0021-9991(81)90128-5.

[43] Brooks, A. N., and Hughes, T. J., "Streamline Upwind/Petrov-Galerkin Formulations for Convection Dominated Flows with Particular Emphasis on the Incompressible Navier-Stokes Equations," *Computer Methods in Applied Mechanics and Engineering*, Vol. 32, No. 1-3, 1982, pp. 199–259. https://doi.org/10.1016/0045-7825(82)90071-8.

[44] Wood, S. L., Jacobson, K., Jones, W. T., and Anderson, W. K., "Sparse Linear Algebra Toolkit for Computational Aerodynamics," *AIAA Scitech 2020 Forum*, American Institute of Aeronautics and Astronautics, Orlando, FL, 2020. https://doi.org/10.2514/6.2020-0317.

[45] Shur, M., Spalart, P., Strelets, M., and Travin, A., "Detached-Eddy Simulation of an Airfoil at High Angle of Attack," *Engineering Turbulence Modelling and Experiments 4*, Elsevier, 1999, pp. 669–678. https://doi.org/10.1016/B978-008043328-8/50064-3.

[46] Atkins, H. L., "Simulations of Compressible Taylor-Green Flow by a Discontinuous Galerkin Method," *46th AIAA Fluid Dynamics Conference*, American Institute of Aeronautics and Astronautics, Washington, D.C., 2016. https://doi.org/10.2514/6.2016-3330.

[47] Simon, F., Deck, S., Guillen, P., and Sagaut, P., "Reynolds-Averaged Navier-Stokes/Large-Eddy Simulations of Supersonic Base Flow," *AIAA Journal*, Vol. 44, No. 11, 2006, pp. 2578–2590. https://doi.org/10.2514/1.21366.

[48] Ashton, N., Batten, P., Skaperdas, V., and Holst, K. R., "High-Lift Prediction Workshop 5: Hybrid RANS/LES Technology Focus Group Summary," *AIAA SCITECH 2025 Forum*, American Institute of Aeronautics and Astronautics, Orlando, FL, 2025. https://doi.org/10.2514/6.2025-0048.

[49] Mouton, S., Charpentier, G., and Lorenski, A., "Test Summary of the Full-Span High-Lift Common Research Model at the ONERA F1 Pressurized Low-Speed Wind Tunnel," *AIAA SCITECH 2023 Forum*, American Institute of Aeronautics and Astronautics, National Harbor, MD & Online, 2023. https://doi.org/10.2514/6.2023-0823.

[50] Park, M. A., Alauzet, F., and Michal, T., "HLPW-4/GMGW-3: Mesh Adaptation for RANS Technology Focus Group Workshop Summary," *Journal of Aircraft*, Vol. 60, No. 4, 2023, pp. 1219–1237. https://doi.org/10.2514/1.C037192.